Atmospheric Research 99 (2011) 15–38

Contents lists available at ScienceDirect

Atmospheric Research

journal homepage: www.elsevier.com/locate/atmos

Evaluation of moist processes during intense precipitation in km-scale NWP models using remote sensing and in-situ data: Impact of microphysics size distribution assumptions

Kwinten Van Weverberg [a,b,*], Nicole P.M. van Lipzig [a], Laurent Delobbe [c]

[a] Department of Earth and Environmental Sciences, K.U. Leuven, Belgium
[b] Atmospheric Sciences Division, Brookhaven National Laboratory, Upton, NY, USA
[c] Royal Meteorological Institute, Uccle, Belgium

ARTICLE INFO

Article history:
Received 9 February 2010
Received in revised form 30 July 2010
Accepted 26 August 2010

Keywords:
Atmospheric model evaluation
Intense precipitation
Size distribution assumptions
One-moment bulk microphysics parameterisation

ABSTRACT

This study investigates the sensitivity of moist processes and surface precipitation during three extreme precipitation events over Belgium to the representation of rain, snow and hail size distributions in a bulk one-moment microphysics parameterisation scheme. Sensitivities included the use of empirically derived relations to calculate the slope parameter and diagnose the intercept parameter of the exponential snow and rain size distributions and sensitivities to the treatment of hail/graupel. A detailed evaluation of the experiments against various high temporal resolution and spatially distributed observational data was performed to understand how moist processes responded to the implemented size distribution modifications.

Net vapour consumption by microphysical processes was found to be unaffected by snow or rain size distribution modifications, while it was reduced replacing formulations for hail by those typical for graupel, mainly due to intense sublimation of graupel. Cloud optical thickness was overestimated in all experiments and all cases, likely due to overestimated snow amounts. The overestimation slightly deteriorated by modifying the rain and snow size distributions due to increased snow depositional growth, while it was reduced by including graupel. The latter was mainly due to enhanced cloud water collection by graupel and reduced snow depositional growth. Radar reflectivity and cloud optical thickness could only be realistically represented by inclusion of graupel during a stratiform case, while hail was found indispensable to simulate the vertical reflectivity profile and the surface precipitation structure. Precipitation amount was not much altered by any of the modifications made and the general overestimation was only decreased slightly during a supercell convective case.

1. Introduction

A proper simulation of severe precipitation within numerical weather prediction models requires that moist processes in the atmosphere are adequately represented. An indispensable part in the turnover of water vapour to clouds and precipitation is the parameterisation of microphysical cloud processes. Due to the small scales of processes involved, a large number of simplifications and assumptions on e.g. size distributions of the several hydrometeors have to be made.

Typically, microphysical processes have been represented in numerical models by one-moment bulk (OMB) microphysical schemes, representing a single size distribution on the bulk of the hydrometeor species within a model grid cell and having only one prognostic moment of a hydrometeor's size distribution, being its mixing ratio (third moment if spherical particles are assumed; e.g. Lin et al., 1983; Rutledge and Hobbs, 1983; Cotton et al., 1986). Current advances in microphysics can be subdivided in at least two main directions. A first sophistication involves a higher number of predicted moments, such as the number

* Corresponding author. Atmospheric Sciences Division, Brookhaven National Laboratory, Building 490-D, Upton, NY, USA.
E-mail address: kvweverberg@bnl.gov (K. Van Weverberg).

0169-8095/$ – see front matter © 2010 Elsevier B.V. All rights reserved.
doi:10.1016/j.atmosres.2010.08.017

concentration (zeroth moment; e.g. Ferrier, 1994; Seifert and Beheng, 2006) or the radar reflectivity (sixth moment; e.g. Milbrandt and Yau, 2005). A second direction consists of separating the mass contents in several size categories (bin or spectral microphysical schemes, e.g. Kogan, 1991; Khain et al., 1999; Ovtchinnikov and Kogan, 2000). As it remains unclear what the main drawbacks for many processes are of the way size distributions in OMB schemes are represented, thorough evaluation and sensitivity studies using such schemes remain valuable (e.g. Woods et al., 2007; Cohen and McCaul, 2006), however. OMB microphysics schemes remain the workhorse in numerical weather prediction to this day, due to their low computational cost.

Many of the studies to OMB microphysical parameterisations over the past decade were conducted for either warm season convection or frontal stratiform precipitation and had a focus on a single microphysical parameter only. Often that parameter was concerned with hail/graupel in studies on convection (Gilmore et al., 2004; McCumber et al., 1991; Smedsmo et al., 2005) and with snow in studies on frontal stratiform precipitation (Colle et al., 2005; Woods et al., 2007). In operational weather forecasting a single model set up is needed which is providing good simulation for both convective and stratiform situations. For that reason it is interesting to understand what impact a model modification made to improve the moist processes under a certain synoptic situation has in other synoptic situations. Furthermore, most of the studies to the influence of microphysical processes on convective storms have been conducted for idealised conditions, initialising the model with a single sounding. While such studies are more straightforward to interpret, they have the disadvantage that they cannot be easily verified against observational data. In recent years, many efforts have been done to obtain spatially distributed observational data with high temporal resolution from spaceborne and ground-based remote sensors, such as satellite and weather radar, largely increasing knowledge on the three-dimensional atmospheric conditions during intense precipitation events.

This research discusses a number of experiments in which size distribution assumptions of a typical OMB microphysical scheme have been more realistically represented for both stratiform and convective intense precipitation situations. Using a broad range of high resolution observational data this research wants to gain more insight in to what extent a more realistic representation of the size distribution assumptions also leads to a model improvement of the representation of moist processes during intense precipitation events. In this work our primary focus is on the spatial scale and not on the temporal scale. A detailed description of the model setup, the cases studied and the available observational data products is given in Section 2. Section 3 provides an overview of the microphysics experiments and results of these experiments are compared against observational data in Section 4. Conclusions and issues for further research are discussed in Section 5.

2. Model setup and observational data

2.1. ARPS description

ARPS is a nonhydrostatic mesoscale meteorological model developed at the University of Oklahoma (Xue et al., 2000, 2001). The finite-difference equations of the model are discretised on an Arakawa C-grid, employing a terrain-following coordinate in the vertical direction. Advection is solved with a fourth-order central differencing scheme and leapfrog time stepping. Land surface processes are parameterised following Noilhan and Planton (1989). The model was applied using one-way grid nesting with two levels. Data on a 0.25° horizontal resolution from the global operational model operated by the European Centre for Medium-Range Weather Forecasts (ECMWF) were used as initial conditions and as 6-hourly lateral boundary conditions for the model run with a 9-km grid spacing and a domain size of 1620×1620 km. Within this domain, a smaller domain centred over Belgium and covering 540×540 km with a 3-km grid spacing was nested. An overview of the model domain is shown in Fig. 1. In all simulations, 50 levels were used in the vertical with a spacing of 20 m near the surface, increasing to 1 km near the upper-model boundary, which was located at a 20-km altitude. All simulations were initialised with a 12 h spin-up period, beginning at 1200 UTC on the previous day. All of the analysis in the following sections is concerned with the 0000 UTC – 2400 UTC period, excluding the spin-up period, if not stated otherwise. Turbulence was represented by the 1.5-order turbulent kinetic energy (TKE) model, and Sun and Chang (1986) parameterisation for the convective boundary layer. The Kain-Fritsch (Kain and Fritsch, 1993) cumulus parameterisation was used in the largest domain, while convection was explicitly simulated at the smaller domain. Cloud microphysics was parameterised following Lin et al. (1983) including five hydrometeor types (cloud water, cloud ice, rain water, snow and hail). In order to suppress numerical noise a fourth order monotonic computational mixing was applied, following Xue (2000).

2.2. Case description

In order to assess the impact of more realistic size distribution assumptions in a bulk microphysical scheme under different synoptic conditions three cases were selected with a very different nature of processes leading to heavy precipitation. In a first case (further referred to as the stratiform case) precipitation was initiated by large-scale uplift during a classical warm- and cold-frontal overpass. Further two cases of severe convection were selected, one having strong mid-level wind shear and moderate buoyancy, being a typical environment for supercell thunderstorms (further referred to as the supercell convective case) and the other having no vertical wind shear but strong buoyancy favouring multicell thunderstorms (further referred to as the convective multicell case). A detailed description of the synoptic and mesoscale features of these three cases is provided in the next paragraphs.

2.2.1. Frontal stratiform case

On 23 November 2006 a classical warm frontal system, followed by an active cold front moved over Belgium from the West, bringing long enduring rain for most of the day, intensifying in the late afternoon during cold front passage. At the 500 hPa level (Fig. 2a), the main feature in the North Atlantic was a trough extending between Greenland and Iceland which was strongly amplifying from 22 November to 24 November. At the same time a strong jet streak developed in the baroclinic zone south of the trough with wind speeds exceeding 85 m s^{-1}.

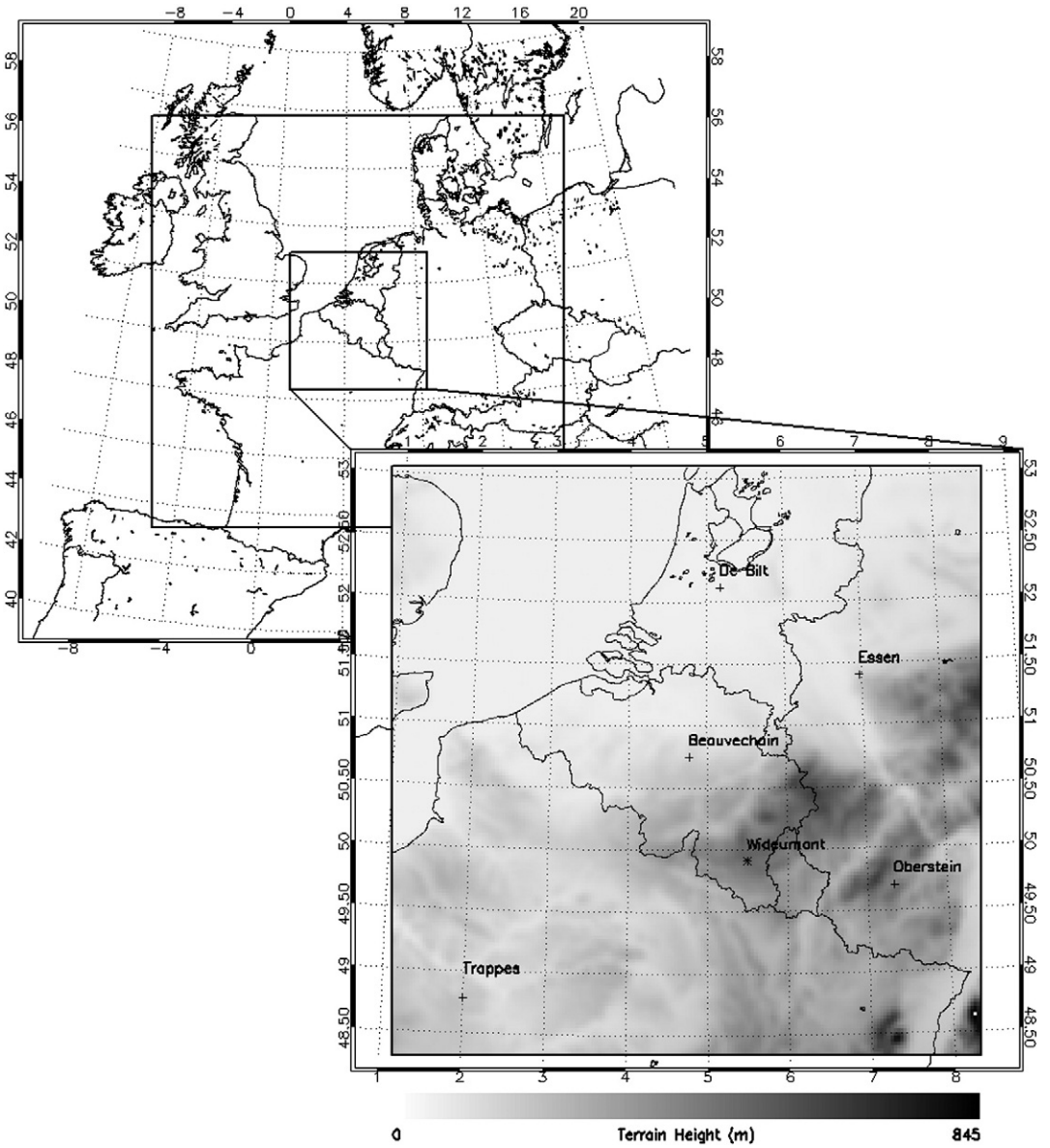

Fig. 1. Model domains used for all experiments. Successive 9- and 3-km nested domains are denoted by bold rectangles (top left). The inset shows the terrain height of the 3-km domain as well as the locations of the five sounding stations mentioned in the text and the location of the Radar of Wideumont. Numbers in the margins indicate latitudes and longitudes.

At the surface a deep depression was positioned southwest of Iceland on 22 November 0000 UTC with rapidly occluding fronts. One of the occluded fronts moved over Belgium late in the evening on 22 November. At the same time, a small surface low associated with the left exit region of the jet streak was showing rapid deepening. From 22 November 0000 UTC to 23 November 0000 UTC the depression deepened from 1007 to 964 hPa while moving from the mid North Atlantic to Ireland, and massively advected warm air across Western Europe (temperatures at 850 hPa went up from about -2 °C to over 5 °C from 0000 UTC on 22 November to 1200 UTC on 23 November near Belgium). The surface warm front associated with this depression reached Belgium just after midnight on 23 November, while the more intense cold front moved in from the West around noon, bringing rain over most of the afternoon. As the cold front started to be positioned more and more along the main upper level flow, its eastward progression slowed down and light to moderate rain lasted for more than 14 h leading to accumulations over 40 mm locally in the south of Belgium.

2.2.2. Supercell convective case

During the afternoon of 1 October 2006 several tornadic supercell thunderstorms developed over Northern France and were advected over Belgium, causing severe damage. A trough at the 500 hPa level extended over the British Isles with an Upper Level Low (ULL) across Ireland and a ridge

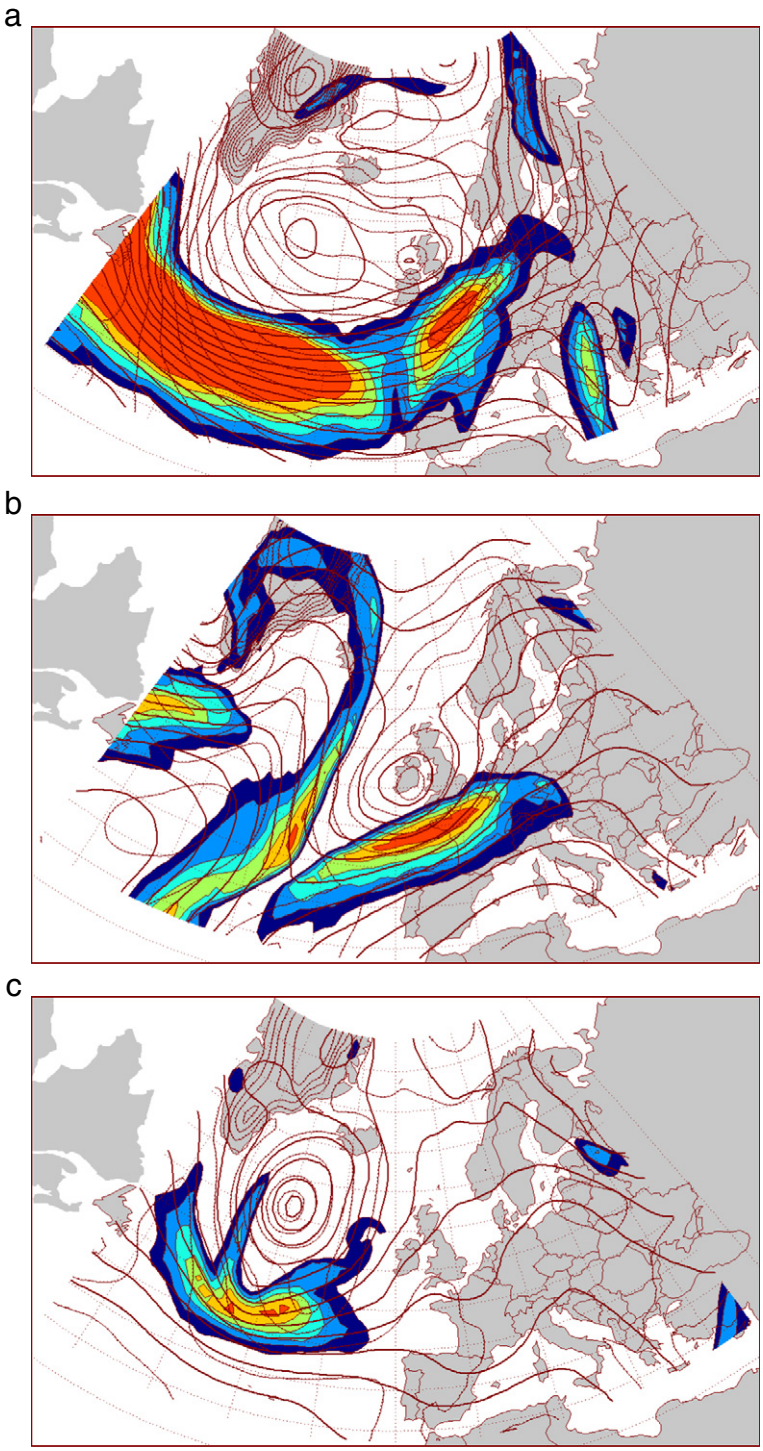

Fig. 2. ECMWF operational analysis at 1200 UTC for the (a) stratiform case, (b) supercell case and (c) multicell case. Color shading indicates scalar wind velocity at 300 hPa (contours drawn each 5 m s^{-1} starting from 30 m s^{-1}). Thick contour lines denote the 500 hPa geopotential height level (contours drawn each 5 dam) and thin contours denote the surface pressure (contours drawn each 5 hPa).

extending from Southern Europe until Eastern Europe, as is represented on Fig. 2b. Between the ULL and the ridge a strong gradient was obvious, leading to the development of a strong jetstreak with winds up to 60 m s^{-1} at 200 hPa. The left exit region of the jet streak was positioned over Belgium during the afternoon. At the surface level, an occlusion,

connected to a low pressure area beneath the ULL passed across Belgium during the forenoon preceding unstable air masses advected from Northern France. While the thermodynamic instability, based on sounding data at 1200 UTC in Trappes (France, Fig. 1), was only moderate with surface-based Convective Available Potential Energy (CAPE) values around 1000 J kg^{-1} and surface-based Lifted Index (LI) values around -3 K, the dynamical built-up of the atmosphere was much more exceptional as significant vertical wind shear was present. The low-level vertical wind shear reached values up to 12 m s^{-1}, while the 0–6 km shear amounted to 28 m s^{-1}. Storm Relative Helicity (SRH) values reached values up to 210 m^2 s^{-2}. According to Groenemeijer and van Delden (2007) these are typical values across North-Western Europe for tornado-producing thunderstorms. Onset of the supercell development in Northern France was around 1400 UTC. Several supercell storms lasted more than 5 h and by then had reached the Netherlands and Germany. Localised precipitation accumulations up to 40 mm, large hail and several tornadoes were reported during this period.

2.2.3. Multicell convective case

Downstream of an intense upper-level longwave trough over the eastern Atlantic, warm air advection occurred over large parts of Western-Europe at 28 July 2006. Beneath a weak upper-level trough positioned near the Belgium, a near-surface moisture convergence zone developed extending from Central France across Belgium until the Netherlands, which led to convection initiation in the deeply unstable air masses during the afternoon (Fig. 2c). As the convergence line was almost stationary during the day, high precipitation accumulations up to 100 mm were reported in this area. East of the moisture convergence line widespread multicell convection initiated from noon on with localised high precipitation accumulation in the east of Belgium and the west of Germany. Surface-based CAPE reached high values up to more than 2000 J kg^{-1} and surface-based LI amounted to about -6 K in De Bilt (the Netherlands, Fig. 1) at 1200 UTC. Vertical wind shear and SRH showed only low values, whereas the Bulk Richardson Number value of 338 favoured multicell storm development. The first thunderstorms along the convergence line appeared at 1100 UTC and remained active until 2000 UTC. Severe convection in this case was obviously mainly driven by favourable thermodynamic instability while there was no significant vertical wind shear.

2.3. Observational data

In order to perform a thorough evaluation of the microphysics sensitivity experiments, we applied the so-called model-to-observation approach (Chevallier and Bauer, 2003; Schröder et al., 2006), in which synthetic observations are derived from the model variables. This approach is favoured because errors associated with the retrieval of model variables from remotely sensed observations (observation-to-model approach) are much more difficult to characterise as a lot of assumptions concerning the atmospheric state have to be made, which are known for the simulated atmosphere. Particle size distributions e.g. are not known in observed atmospheres and introduce a lot of uncertainty in the retrieval of hydrometeor quantities from observed reflectivities. In the model, however, it is well known what those size distributions are and hence the inverse method of calculating reflectivities from the model variables is less prone to uncertainties.

2.3.1. Sounding data

Observed vertical profiles of water vapour were obtained for five sounding stations within the simulation domain, being Beauvechain (50.75 N, 4.77 E), Trappes (48.77 N, 2.02 E), Oberstein (49.70 N, 7.33 E), De Bilt (52.10 N, 5.18 E) and Essen (51.40 N, 6.97 E). The locations of these stations are denoted on Fig. 1. In all stations, radio soundings were launched twice a day, at 0000 UTC and at 1200 UTC, except for Beauvechain where only one sounding was launched at 0000 UTC. Vertically integrated water vapour at these stations is compared against the modelled vertically integrated water vapour at the grid cell located closest to the station position.

2.3.2. Satellite data

In order to evaluate simulated cloud phase (q_c, q_i and q_s), cloud optical thickness (COT) was used, derived from SEVIRI (Spinning Enhanced Visible and Infrared Radiometer) onboard the geostationary METEOSAT satellites (Meteosat-8, -9). COT was derived by the EUMETSAT Satellite Application Facility on Climate Monitoring (CM-SAF, Schulz et al., 2009), using the algorithms described in Roebeling et al. (2006), for the multicell convective and the stratiform case. During the supercell convective case Meteosat-8 entered sleeping mode and hence we used the COT derived by the World Data Center for Remote Sensing of the Atmosphere (WDC-RSAT) using the AVHRR Processing scheme Over cLouds, Land and Ocean (APOLLO, discussed in Saunders and Kriebel, 1988) applied on Meteosat-9 SEVIRI. COT calculation is applied to each grid cell of a satellite scene and is available on a 3 km horizontal resolution at the sub-satellite point with an image repeat cycle of 60 min. As the visual channel is used for COT calculation, only daytime hours are included in the further analysis. Considerable uncertainty exists in the COT retrieval from satellite. By comparison against pyranometer data from Cabauw, Karlsson et al. (2005) found a good correlation of 0.85 of the daily average COT, although, at certain times large differences could be found due to mismatches in collocation and the sensitivity of the pyranometer retrieval to inhomogeneities in the cloud properties. In order to avoid mismatches due to mislocations we decided to perform model evaluation only by means of integrated methods, such as by comparing the daily integrated simulated and observed frequency distribution.

COT in ARPS is calculated for each hydrometeor separately, following a routine developed at the National Aeronautics and Space Administration (NASA) Goddard Cumulus Ensemble Modelling Group (Tao et al., 2003). For liquid (water) clouds and hail, COT in the visible region is parameterised based on Sui et al. (1998) following Fu and Liou (1993) assuming spherical droplets:

$$\tau_c = 1.5 \times \int \frac{q_c}{R_{ec}} dz, \tag{1}$$

$$\tau_r = 1.5 \times \int \frac{q_r}{R_{er}} dz, \tag{2}$$

$$\tau_h = \int \frac{q_h}{R_{eh}} dz, \quad (3)$$

where q_c, q_r and q_h are the mixing ratios (in kg kg^{-1}) of cloud water, rain and hail respectively and effective radii (in cm) $R_{ec}=0.0015$, $R_{er} = \frac{3.}{(\pi N_{0r}\rho_r / \rho q_r)^{0.25}}$ and $R_{eh} = \frac{3.}{(\pi N_{0h}\rho_h / \rho q_h)^{0.25}}$. For cloud ice and snow, COT is parameterised based on formula derived for cirrus ice crystals by Fu and Liou (1993):

$$\tau_{is} = \int 10^4 \times (q_i + q_s) \times \left(0.006656 + \frac{3.686 \times 10^{-4}}{R_{eis}}\right) dz \quad (4)$$

where q_i and q_s are the mixing ratio (kg kg^{-1}) of cloud ice and snow respectively and $R_{eis}=0.0125$ if temperature (T) is above 243.16 K, $R_{eis}=0.0025$ if temperature is below 223.16 K and $R_{eis}=0.0125+(T-243.16)*0.0005$ if temperature is between 223.16 and 243.16 K. Total COT is defined as the sum of all components described in Eqs. (1)–(4). The empirical coefficients -0.006656 and 3.3686×10^{-4} are determined by Fu and Liou (1993) from fitting different numerical scattering and absorption programs to observed snow size distribution data.

2.3.3. Volume radar data

Three-dimensional fields of precipitating hydrometeors can be compared using radar-derived reflectivity values. Volume radar data from the C-band weather radar of Wideumont were derived from a 10-elevation reflectivity scan performed every 15 min and interpolated to the ARPS grid. It is well known that C-band radars suffer from attenuation already at moderate rain rates. During and shortly after rainfall on the radar radome, attenuation might become even more of a problem. Therefore, it was chosen to only include data from within a radius of 150 km from the radar position in all further analysis and to perform evaluation using time-integrated methods, rather than comparing individual snap shots. Equivalent reflectivity data, Z_e, in mm^6 m^{-3}, in ARPS were calculated following Tong and Xue (2008), based on formulations by Smith et al. (1975) assuming Rayleigh scattering for rain, dry snow, wet snow, dry hail and wet hail, yielding:

$$Z_r = \frac{720 \times 10^{18} N_{0r}}{\lambda_r^7}, \quad (5)$$

$$Z_{sd} = \frac{K_i^2 \rho_s^2 720 \times 10^{18} N_{0s}}{K_w^2 \rho_i^2 \lambda_s^7}, \quad (6)$$

$$Z_{sw} = \frac{720 \times 10^{18} N_{0s}}{\lambda_s^7}, \quad (7)$$

$$Z_{hd} = \frac{0.19 \times 720 \times 10^{18} N_{0h}}{\lambda_h^7}, \quad (8)$$

$$Z_{hw} = \left(\frac{720 \times 10^{18} N_{0h}}{\lambda_h^7}\right)^{0.95}, \quad (9)$$

where Z_r, Z_{sd}, Z_{sw}, Z_{hd} and Z_{hw} are reflectivity factors for rain, dry snow, wet snow, dry hail and wet hail respectively, and N_{0r}, N_{0s}, N_{0h}, λ_r, λ_s and λ_h are the intercept and slope parameters of the exponential size distributions of rain, snow and hail respectively. Total Z_e is the sum of each of the components described above (Eqs. (5)–(9)). Reflectivity Z, is calculated from Z_e by

$$Z = 10 log_{10}(Z_e), \quad (10)$$

The reflectivity data in ARPS were calculated for each model level. Data beyond 150 km from the location of the Wideumont radar and below the lowest beam elevation were omitted from the further analysis.

2.3.4. Radar-rain gauge merging product

Surface precipitation observations are obtained from the C-band weather radar in Wideumont (Fig. 1) operated by the Royal Meteorological Institute of Belgium and from a dense network of rain gauges (1 per 135 km^2) operated by the hydrological service of the Walloon region. Radar-based precipitation estimates are derived from a 5-elevation reflectivity scan performed every 5 min. The processing of the radar data and various strategies for merging radar observations with rain gauge measurements are presented in Goudenhoofdt and Delobbe (2009). In this study, radar and gauge observations have been combined using a simple mean field bias adjustment. Mean bias and mean absolute error using this method were found to be in the order of 0.039 dB and 1.5 mm respectively during a 4-year verification against an independent set of rain gauge stations (Goudenhoofdt and Delobbe, 2009). The 24 h precipitation accumulations for the three cases have been calculated using this method and were aggregated to the ARPS grid. As radar suffers from many issues regarding the quality of its returned power (e.g. attenuation), mainly at large distances from the radar itself, data from beyond 150 km from the radar position were omitted from the further analysis in both the observed and the simulated fields.

3. Experimental design

The microphysics scheme used in the control experiment of this study is the five-hydrometeor type (cloud water, cloud ice, rain, snow and hail) OMB scheme developed by Lin et al. (1983). All precipitating hydrometeors are represented by exponential size distributions of the form

$$N_x(D) = N_{0x}\, exp(-\lambda_x D_x), \quad (11)$$

where N is the number of particles per unit volume per unit size range, D is the maximum dimension of a particle and N_{0x} and λ_x are the intercept and slope of the exponential size distribution, respectively. The subscript x denotes the water specie (rain, snow or hail). While the intercept parameter is assumed constant, slope parameters, assuming all hydrometeors to be constant density spheres, are determined by

$$\lambda_x = \left(\frac{\pi \rho_x N_{0x}}{\rho_{air} q_x}\right)^{0.25} \quad (12)$$

where ρ_x is the hydrometeor density, q_x is the hydrometeor mixing ratio and ρ is the air density. Many of the assumptions made in this scheme are contradicted by observational studies and could be major sources of error in the QPF.

First, intercept parameters of the rain and snow size distributions are observed to vary over several orders of magnitude in the atmosphere (Waldvogel, 1974; Houze et al., 1979). Second, schemes such as the Lin et al. (1983) scheme apply mass-diameter (m-D) relationships for constant density spheres for the calculation of the slope parameter of all hydrometers, while many observational studies suggest different m-D relationships for snow and graupel (e.g. Locatelli and Hobbs, 1974). Third, hail and snow in the scheme are weighted towards large hailstones and fast falling graupel-like snow respectively, which might be a good approximation for typical thunderstorms over the Midwest United Sates, but could be problematic under different atmospheric conditions and in other regions.

In order to understand the implications of these drawbacks of the microphysics schemes for the simulation of moist processes and surface precipitation in the atmosphere, we have set up two sensitivity experiments for each case. In operational weather forecasting a single setting of the microphysics assumptions is required which should provide good guidance in all synoptic conditions. Both experiments are designed to understand what the implications are of a model modification specifically set up for a certain synoptic situation for other synoptic situations. A first experiment is what would be considered an improved setting for convective situations, further referred to as the ExpGRHA experiment. In this experiment only the rain and snow size distribution assumptions were modified, while the assumptions for large hail were kept unchanged from the original Lin et al. (1983) scheme. The more realistic assumptions for the rain and snow size distributions included a mixing ratio dependency of N_{or}, following Zhang et al. (2008) and a temperature dependency for N_{0s}, following Houze et al. (1979), yielding respectively

$$N_{0r} = 0.07106(1000\rho q_r)^{0.648} \tag{13}$$

$$N_{0s} = 0.02exp[0.12(T_0 - T)] \tag{14}$$

Further we calculated λ_s using m-D relations observed by Locatelli and Hobbs (1974) instead of assuming constant density sphere, following Woods et al. (2007):

$$\lambda_x = \left(\frac{a_m N_{0x}\Gamma(b_m+1)}{\rho_{air} q_x}\right)^{1/(b_m+1)}, \tag{15}$$

where a_m and b_m are the empirically derived constants for the m-D relation $m_x = a_m D_x^{b_m}$ of fast falling graupel-like snow observed by Locatelli and Hobbs (1974). Using this m-D relationship and the respective V-D power-law relationship $V_x = a_v D_x^{b_v}$ for graupel-like snow observed by Locatelli and Hobbs (1974) mass-weighted terminal fall speed V_x of snow can be described as (Woods et al., 2007):

$$V_x = \frac{a_v\Gamma(b_m + b_v + 1)}{\lambda_x^{b_v}\Gamma(b_m+1)} \tag{16}$$

The second experiment we conducted can be considered an improved setting for stratiform precipitation conditions and is further referred to as the ExpDSGR. The rain size distribution assumptions were modified as in the ExpGSHA, but for the calculation of λ_s and V_s we implemented now the m-D and V-D relations for dendritic snow as observed by Cox (1988). We assumed that for gentle uplift in a frontal stratiform environment this would be a better representation than the graupel-like fast precipitating snow species as applied in the ExpGSHA, as suggested by e.g. Cox (1988) or Jiusto and Bosworth (1971). Furthermore, we replaced the formulation for large hailstones by formulations for small graupel, having a larger constant intercept parameter and a lower density. The calculation of λ_G and V_G was done following experimental m-D and V-D relations for dense lump graupel as observed by Locatelli and Hobbs (1974) instead of assuming constant density spheres in the original Lin et al. (1983) formulations.

A full description of all modifications made in the sensitivity experiments is given in Table 1. The impact of the modifications made on the sedimentation velocities of the precipitating hydrometeors is given in Fig. 3. The influence of our modifications on the mass weighted rain fall speed (Fig. 3a) shows a decreased fall speed when the rain mixing ratio is above 1.2 g kg^{-1} and an increased when it is below this value. Mass weighted snow fall speeds not only depend on the mixing ratio of snow, but also on the temperature when microphysics is modified. In the ExpDSGR experiment snow fall speeds are decreased at all temperatures as compared to the CONTROL with lowest fall speeds at coldest temperatures. In the ExpGRHA experiment snow fall speeds are increased for temperatures above 240 K and decreased below (Fig. 3b). The graupel fall speeds in the ExpDSGR experiment are about 7 times as small as those in the other experiments (Fig. 3c).

4. Results

In the following sections, the effect of modifying microphysical size distribution assumptions on the representation of moist processes under various synoptic conditions will be evaluated systematically by comparison against remotely sensed and in situ observational data.

4.1. Sounding derived integrated water vapour

4.1.1. Stratiform case

All water being converted from one phase to another within a microphysics scheme ultimately originates from atmospheric water vapour. Before evaluating and analysing the influence of our experiments on the microphysical conversions, it is hence desirable to first investigate if atmospheric water vapour is well represented in the simulations and if the size distribution assumptions lead to differences in the amount of water vapour consumed by the microphysics scheme. Table 2 summarises the statistics of vertically integrated water vapour (IWV) as derived from sounding information and for all experiments during the three simulated cases. It is clear that IWV does not show a systematic bias in any of the size distribution experiments during the stratiform case. The domain total net vapour consumption by the microphysics scheme accumulated over

Table 1
Formulations for the intercept parameter (N_0), slope parameter (λ) and terminal fall velocity (V) for all precipitating hydrometeors.

	CONTROL	ExpGRHA	ExpDSGR
N_{0r}	0.08	$0.07106(10^3\rho q_r)^{0.648}$	$0.07106(10^3\rho q_r)^{0.648}$
	(Marshall and Palmer, 1948)	(Zhang et al., 2008)	(Zhang et al., 2008)
λ_r	$\left(\frac{\pi\rho_r N_{0r}}{\rho q_r}\right)^{0.25}$	$\left(\frac{\pi\rho_r N_{0r}}{\rho q_r}\right)^{0.25}$	$\left(\frac{\pi\rho_r N_{0r}}{\rho q_r}\right)^{0.25}$
V_r	$\frac{2115\Gamma(4+0.8)}{6\lambda_t^{0.8}}\left(\frac{\rho_0}{\rho}\right)^{1/2}$	$\frac{2115\Gamma(4+0.8)}{6\lambda_t^{0.8}}\left(\frac{\rho_0}{\rho}\right)^{1/2}$	$\frac{2115\Gamma(4+0.8)}{6\lambda_t^{0.8}}\left(\frac{\rho_0}{\rho}\right)^{1/2}$
	(Liu and Orville, 1969)	(Liu and Orville, 1969)	(Liu and Orville, 1969)
N_{0s}	0.03	$0.02\exp[0.12(T_0-T)]$	$0.02\exp[0.12(T_0-T)]$
	(Gunn and Marshall, 1958)	(Houze et al., 1979)	(Houze et al., 1979)
λ_s	$\left(\frac{\pi\rho_s N_s}{\rho q_s}\right)^{0.25}$	$\left(\frac{0.0074N_{0s}\Gamma(2.1+1)}{\rho q_s}\right)^{1/(2.1+1)}$	$\left(\frac{0.0069N_{0s}\Gamma(2+1)}{\rho q_s}\right)^{1/(2+1)}$
	(Lin et al., 1983)	(Locatelli and Hobbs, 1974)	(Cox, 1988)
V_s	$\frac{152.93\Gamma(4+0.25)}{6\lambda_s^{0.25}}\left(\frac{\rho_0}{\rho}\right)^{1/2}$	$\frac{209.60\Gamma(0.28+2.1+1)}{\lambda_s^{0.28}\Gamma(2.1+1)}$	$\frac{148.07\Gamma(0.527+2+1)}{\lambda_s^{0.527}\Gamma(2+1)}$
	(Locatelli and Hobbs, 1974)	(Locatelli and Hobbs, 1974)	(Cox, 1988)
N_{0h}	0.0004	0.0004	4.000
	(Federer and Waldvogel, 1975)	(Gilmore et al., 2004)	(Gilmore et al., 2004)
λ_h	$\left(\frac{\pi\rho_h N_h}{\rho q_h}\right)^{0.25}$	$\left(\frac{\pi\rho_h N_h}{\rho q_h}\right)^{0.25}$	$\left(\frac{0.0702N_{0h}\Gamma(2.7+1)}{\rho q_h}\right)^{1/(2.7+1)}$
	(Lin et al., 1983)	(Lin et al., 1983)	(Locatelli and Hobbs, 1974)
V_h	$\frac{\Gamma(4.5)}{6\lambda_h^{0.5}}\left(\frac{4g\rho_h}{3C_D\rho}\right)^{1/2}$	$\frac{\Gamma(4.5)}{6\lambda_h^{0.5}}\left(\frac{4g\rho_h}{3C_D\rho}\right)^{1/2}$	$\frac{234.42\Gamma(0.37+2.7+1)}{\lambda_h^{0.37}\Gamma(2.7+1)}$
	(Wisner et al., 1972)	(Wisner et al., 1972)	(Locatelli and Hobbs, 1974)

24 h is similar for the CONTROL and ExpGRHA, but is slightly lower during the ExpDSGR (Table 2).

The low sensitivity of net water vapour consumed by microphysical processes balances a rather strong sensitivity of the magnitude of individual conversion processes involving water vapour. Fig. 4a provides an overview of all microphysical gain and loss terms (in kg) during the stratiform case for the 5 hydrometeor species and water vapour. These conversion terms represent accumulated values over 24 h and over the whole domain (excluding 20 grid cells from the boundary at each side of the domain). It is clear that the individual conversion terms related to water vapour differ considerably. In the ExpGRHA experiment, the depositional growth of snow (Psdpv) nearly doubles as compared to the CONTROL. This is compensated for by a strong depletion of cloud water by evaporation (Pvevw) and hence the vapour consumed by the microphysics scheme is similar in both sensitivity experiments. Weighting the size distribution assumptions to those more typical of stratiform precipitation (ExpDSGR) leads to a decrease in depositional growth of snow (Psdpv), which is compensated for by increased cloud water condensation (Pwcdv) and decreased cloud water evaporation (Pvevw).

4.1.2. Convective cases

During the supercell convective case, no IWV bias is present during the precipitation period in any of the experiments, while a slight positive IWV bias can be noticed in all experiments during the multicell case (Table 2). The net vapour consumed by the microphysics scheme is somewhat decreased in both the ExpGRHA and ExpDSGR in contrast to the CONTROL. This is caused by a decreased cloud water condensation in ExpGRHA, which is not fully compensated by increased depositional growth of snow. On the other hand, in ExpDSGR, the large amount of vapour returned to the atmosphere by sublimation of graupel could not be compensated by an increase in condensation of water vapour (Fig. 4b and c). The slight improvement in the positive IWV bias in the ExpDSGR experiment hence cannot be related to consumption by the microphysics scheme and is probably due to precipitation which occurred the night before in ExpDSGR but not in the other experiments.

4.2. MSG-derived cloud optical thickness

4.2.1. Stratiform case

Cloud optical thickness (COT) in the visible spectrum is directly dependent on the amount of cloud water, cloud ice and snow and hence provides a good estimate to evaluate the cloud phase of the microphysics experiments we carried out. Fig. 5 provides the frequency distributions, calculated from hourly snapshots of the observed and simulated cloud optical thickness. Only daytime hours have been included and the 20 grid cells closest to each domain boundary have been excluded. As the satellite cannot discriminate between values above 100, we truncated all simulated values above this value.

It is clear that the COT distribution is weighted too much to the optically thicker clouds in the CONTROL experiment during the stratiform case. Modifying the size distribution assumptions of rain and snow (ExpGRHA experiment) leads to a slightly deteriorated distribution of COT, as a larger fraction of the cloudy grid cells has a COT well above 90. Weighting the size distribution assumptions of snow and graupel to those typical of stratiform precipitation (ExpDSGR experiment) brings the COT distribution much more in

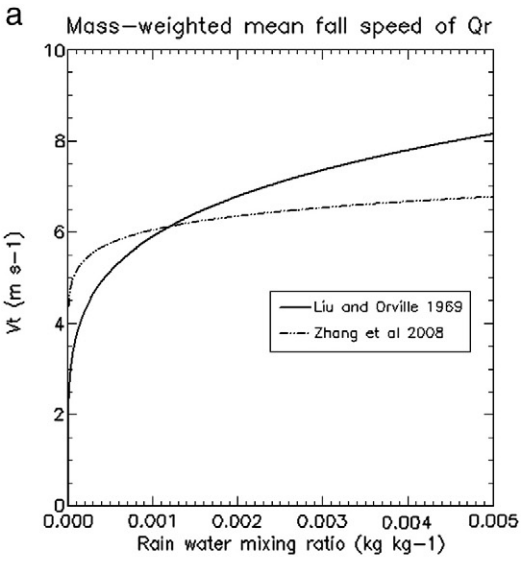

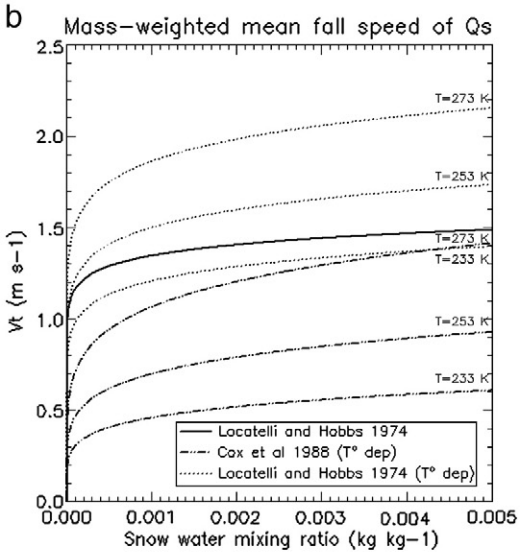

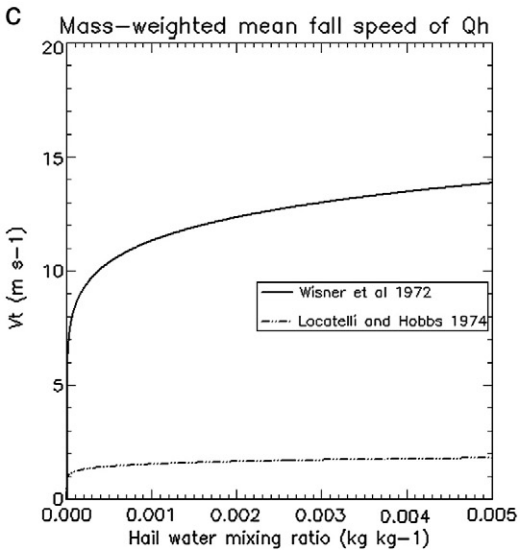

Fig. 3. Sedimentation velocity in function of mixing ratios for (a) rain, (b) snow and (c) hail/graupel for the different formulations used in the experiments. Table 1 summarises which formulations were used in each experiment.

Table 2
Mean integrated water vapor and water vapor bias from the observations for all cases and all experiments, averaged over 5 sounding stations across the domain and over the two launch times (0000 and 1200 UTC).

	Mean IWV (kg m^{-2})	Bias IWV (%)	Net vapour loss (10^{11} kg per 12 h)
Stratiform			
CONTR	21.8	−0.8	30.3
ExpGRHA	21.8	−0.8	31.2
ExpDSGR	21.7	−0.9	27.9
Supercell			
CONTR	25.0	0.1	6.4
ExpGRHA	24.8	−0.1	5.6
ExpDSGR	24.8	−0.1	5.1
Multicell			
CONTR	38.9	2.0	34.0
ExpGRHA	38.2	1.7	33.2
ExpDSGR	37.3	0.8	28.0

Furthermore, net vapour consumption by microphysical processes in all experiments has been provided.

accordance with the observed distribution, although an underestimation appears of the thickest clouds. In order to solve the question as to which of the hydrometeors is responsible for the changes in COT between the different experiments, vertical profiles of cloud ice, cloud water and snow, averaged over time and the domain are given in Fig. 6a. It is clear that snow and graupel are the main species experiencing significant modifications from the sensitivity experiments. In ExpGSHA snow depositional growth significantly increases (Psdpv, Fig. 4a) both because of the empirical m-D relation used (mainly at relatively warm temperatures) and the use of a temperature dependent N_{0s} which results in much more snowflakes at cold temperatures. This confirms findings of e.g. Thompson et al. (2008) who found strongly increased snow growth changing the constant density sphere assumption of snow to an empirical m-D relation. Despite this increased depositional growth of snow (Psdpv, Fig. 4a), snow amounts hardly grow larger in the ExpGRHA experiment as compared to the CONTROL experiment (Fig. 6a). (Note that Fig. 4a provides a time integration and that no snow is left at the end of this integration. Hence *net* snow growth over this integration time is similar between the experiments, as most of it ultimately leaves the model again through losses to the hail and the rain species.) The latter is due to enhanced snow fall speeds in ExpGSHA, mainly at warm temperatures (Fig. 3b). Given the dominance of the snow species in the COT and the strong overestimation of COT in the experiments having large amounts of snow, it is likely that snow amounts are strongly overestimated in both the CONTROL and ExpGRHA experiments.

Snow amounts strongly decrease when applying formulations for snow and graupel which are typical for stratiform precipitation (ExpDSGR experiment), which brings the COT much closer to the observations. Snow depositional growth

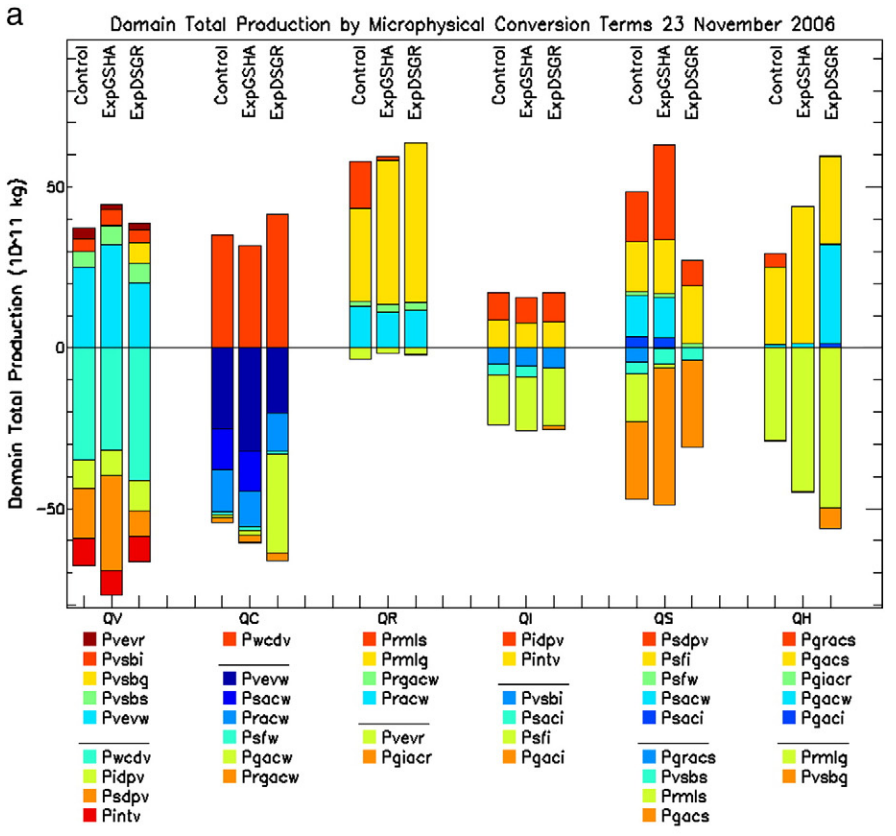
a
Domain Total Production by Microphysical Conversion Terms 23 November 2006
Domain Total Production (10^11 kg)
Control
ExpGSHA
ExpDSGR
QV
QC
QR
QI
QS
QH
Pvevr
Pvsbi
Pvsbg
Pvsbs
Pvevw
Pwcdv
Pidpv
Psdpv
Pintv
Pwcdv
Pvevw
Psacw
Pracw
Psfw
Pgacw
Prgacw
Prmls
Prmlg
Prgacw
Pracw
Pvevr
Pgiacr
Pidpv
Pintv
Pvsbi
Psaci
Psfi
Pgaci
Psdpv
Psfi
Psfw
Psacw
Psaci
Pgracs
Pvsbs
Prmls
Pgacs
Pgracs
Pgacs
Pgiacr
Pgacw
Pgaci
Prmlg
Pvsbg

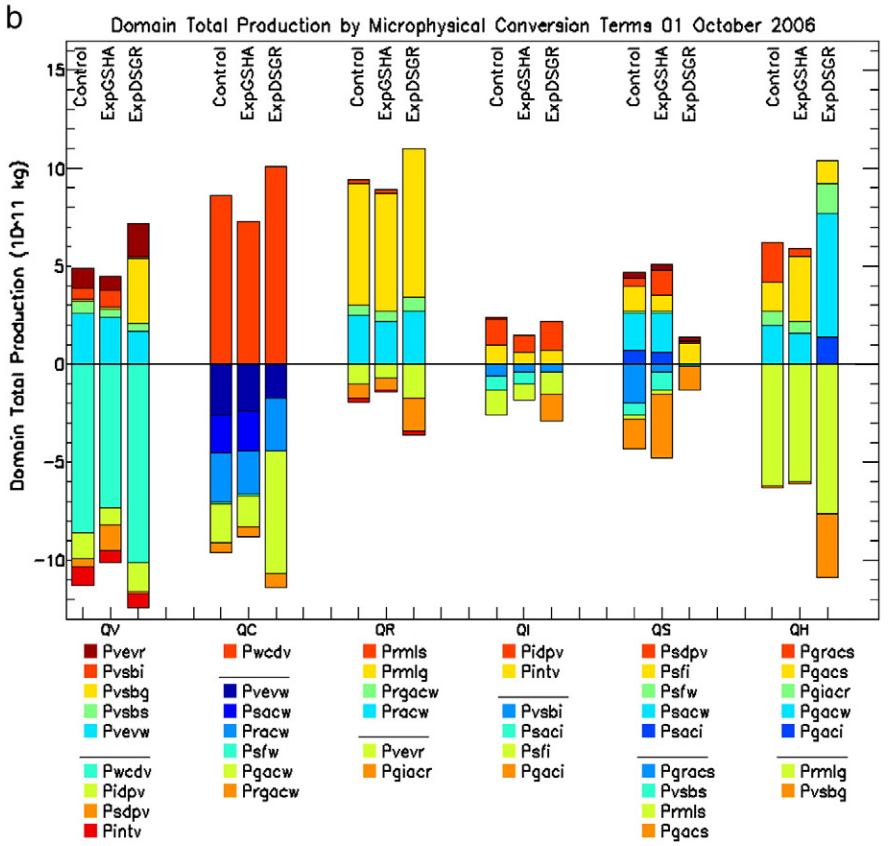
b
Domain Total Production by Microphysical Conversion Terms 01 October 2006
Domain Total Production (10^11 kg)
Control
ExpGSHA
ExpDSGR
QV
QC
QR
QI
QS
QH
Pvevr
Pvsbi
Pvsbg
Pvsbs
Pvevw
Pwcdv
Pidpv
Psdpv
Pintv
Pwcdv
Pvevw
Psacw
Pracw
Psfw
Pgacw
Prgacw
Prmls
Prmlg
Prgacw
Pracw
Pvevr
Pgiacr
Pidpv
Pintv
Pvsbi
Psaci
Psfi
Pgaci
Psdpv
Psfi
Psfw
Psacw
Psaci
Pgracs
Pvsbs
Prmls
Pgacs
Pgracs
Pgacs
Pgiacr
Pgacw
Pgaci
Prmlg
Pvsbg

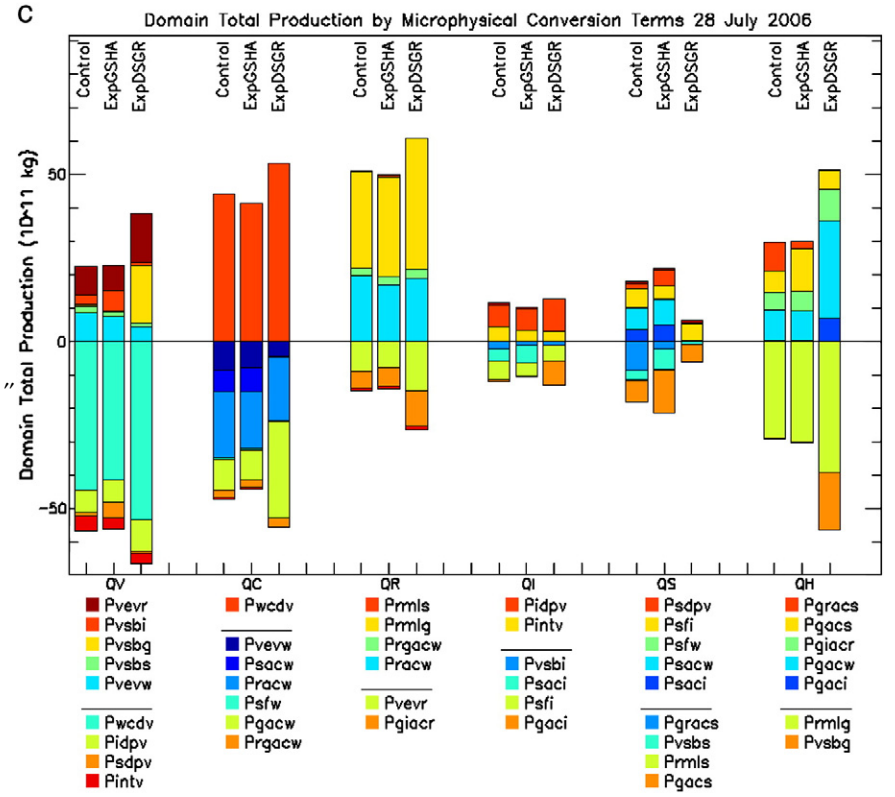

Fig. 4. (a) Total production and loss (10^{11} kg) summed over the domain and over 24 h (0000 UTC–2400 UTC) during the stratiform case for (from left to right) q_v, q_c, q_r, q_i, q_s and q_h and for experiments CONTR, ExpGRHA and ExpDSGR. Legends of the individual conversion processes for a specific hydrometeor are given below the respective hydrometeor graphs. Naming convention is so that the species experiencing gain (loss) is represented by the first (last) letter. The third and fourth letters indicate the type of interaction: ev (evaporation), sb (sublimation), cd (condensation), dp (deposition), nt (initiation), ac (accretion), f (Bergeron process) and ml (melting). When three species are involved, the third letter indicates the accreting species. (b) The same as panel a, but for the supercell convective case from 1200 UTC–1800 UTC and for CONTR, ExpGRHA and ExpDSGR experiments. (c) The same as panel a, but for the multicell convective case from 1200 UTC–1800 UTC and for CONTR, ExpGRHA and ExpDSGR experiments.

(Psdpv) decreases as less snow is available. Indeed, as soon as snow appears, it is collected by graupel (Pgacs), which is also lofted to higher altitudes in the atmosphere. As graupel deposition growth is not parameterised in the Lin et al. (1983) scheme, cloud water condensation (Pwcdv) will be enhanced in order to convert vapour to condensate. As most of this additional cloud water is collected by graupel (Pgacw), total cloud water remains unaffected. Although the total amount of frozen hydrometeors remains similar as in the CONTROL and ExpGSHA experiments, COT decreases as graupel is optically much thinner as compared to snow. Modifications in the size distribution assumptions as presented here hence mainly have an impact on whether the dominant precipitating ice species will be either snow or graupel, while the total glaciation of clouds and precipitation remains highly unaffected. Earlier observational studies tend to suggest that there might be a too excessive glaciation in many simulated midlatitude stratiform cloud systems leading to underestimated amounts of (supercooled) liquid water (Reisner et al., 1998; Thompson et al., 2008 and Solomon et al., 2009).

It can be noticed that cloud ice and cloud water are not much affected by any of the modifications made (Fig. 6a). Again, this could be due to compensating effects (Fig. 4a). In the ExpDSGR experiment more cloud water is lost by riming growth of graupel (Pgacw), which is compensated for by increased condensation (Pwcdv). More cloud water evaporates (Pvevw), which is compensated by decreased riming growth of snow (Psacw) and accretion by rain (Pracw).

4.2.2. Convective cases

During the supercell convective case, the model tends to underestimate the number of grid cells having low COT values, while too many thick clouds occur (Fig. 5). Differences between the different experiments are small in this case, although less optically thick clouds are present in the ExpDSGR.

Vertical hydrometeor profiles are given in Fig. 5b. While cloud water seems to be somewhat more affected in the ExpGRHA as compared to similar size distribution modifications in the stratiform case, it is again mainly the snow content which is significantly altered when compared to the CONTROL experiment. Due to its slower fall speed (Fig. 3) at cold temperatures and its larger number concentration, Psdpv increases in the upper tropospheric levels (Fig. 4b). Cloud water in the ExpGRHA experiment is slightly reduced above the freezing level due to increased Psdpv (Fig. 4b). Around the freezing level, snow sedimentation becomes

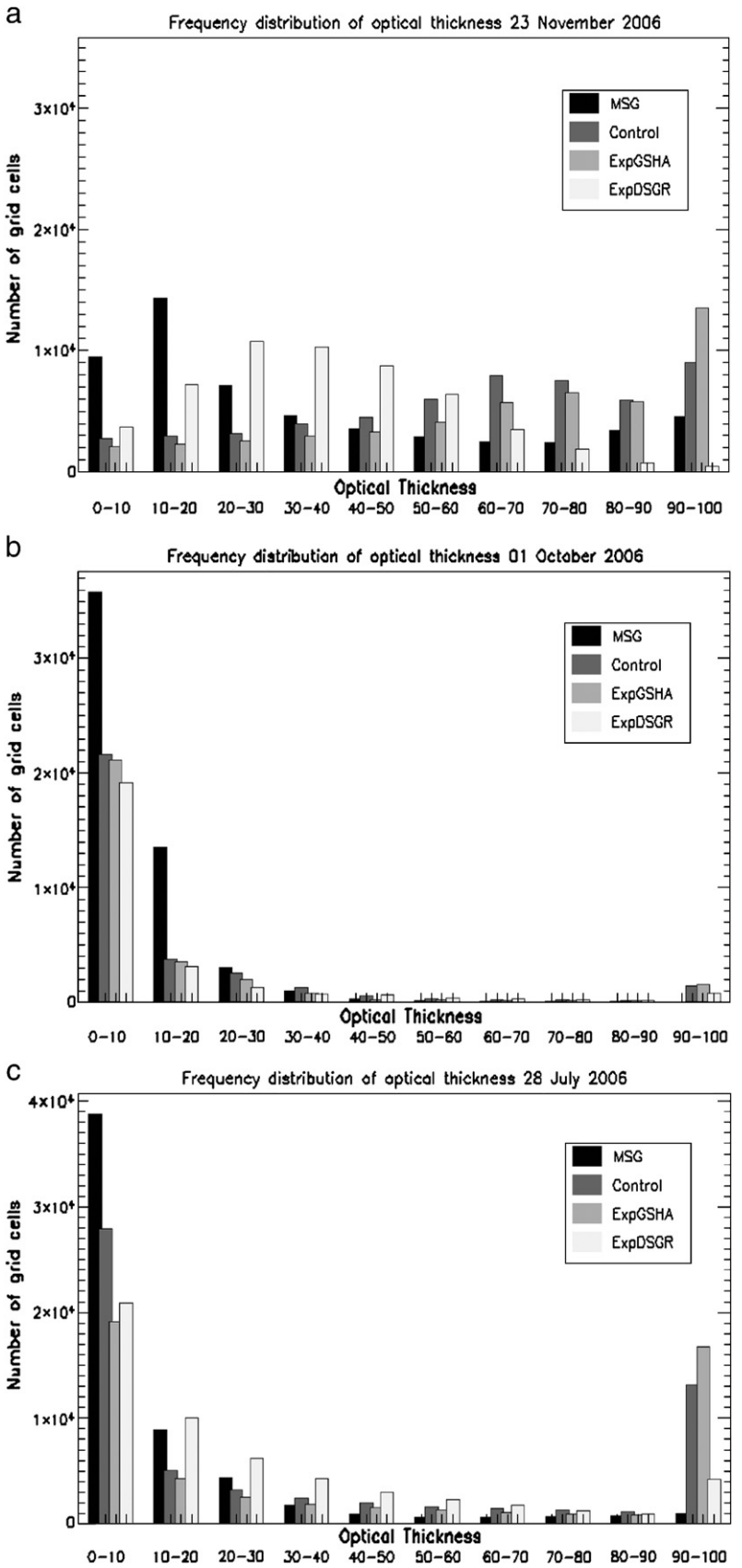
a
Frequency distribution of optical thickness 23 November 2006
MSG
Control
ExpGSHA
ExpDSGR
Number of grid cells
3x10⁴
2x10⁴
1x10⁴
0
Optical Thickness
0–10
10–20
20–30
30–40
40–50
50–60
60–70
70–80
80–90
90–100
b
Frequency distribution of optical thickness 01 October 2006
MSG
Control
ExpGSHA
ExpDSGR
Number of grid cells
3x10⁴
2x10⁴
1x10⁴
0
Optical Thickness
0–10
10–20
20–30
30–40
40–50
50–60
60–70
70–80
80–90
90–100
c
Frequency distribution of optical thickness 28 July 2006
MSG
Control
ExpGSHA
ExpDSGR
Number of grid cells
4x10⁴
3x10⁴
2x10⁴
1x10⁴
0
Optical Thickness
0–10
10–20
20–30
30–40
40–50
50–60
60–70
70–80
80–90
90–100

faster with increasing temperature and hence snow amounts quickly converge to the amounts in the CONTROL experiment in the lower troposphere. In the ExpDSGR experiment, cloud water is dramatically depleted above the freezing level, which is mainly due to strongly increased accretion by graupel (Pgacw, Fig. 4b) and the strongly decreased sedimentation velocity (Fig. 3c). As the enormous amounts of graupel produced in this experiment are lofted to much higher altitudes (Fig. 6b), accretion of snow by graupel (Pgacs) takes place at higher altitudes, depleting snow at an earlier stage in its growth process. Furthermore, riming of cloud water on snow (Psacw), one of the main growth mechanisms in the CONTROL and ExpGRHA experiment, can hardly take place due to strongly reduced amounts of cloud water.

In contrast to the supercell case, there is no clear underestimation of the number of shallow clouds in the multicell case. The overestimation of the number of optically thick clouds is very large again in all experiments. However, improvements occur in the ExpDSGR, while ExpGRHA tends to increase the bias towards too thick clouds. The same mechanisms are at play as in the supercell case (Figs. 4c and 5c). The reason for the overestimation of COT is not easy to trace. It could be that even in convective cases, in which deposition growth of the ice phase is much more marginal in contrast to riming growth, storms are too glaciated. On the other hand, storm updrafts might be too intense due to e.g. the too coarse spatial resolution, leading to more condensation than was observed.

4.3. Radar reflectivity

4.3.1. Stratiform case

C-band radar reflectivity is mainly influenced by hail and rain and to a lesser extent by snow and hence provides a good measure of evaluating the precipitating hydrometeors in the microphysical experiments we carried out. Fig. 7a summarises 3D-volume reflectivity information from observations and all simulations by means of contoured frequency by altitude diagrams (CFADs), which are diagrams representing the variation of reflectivity probability density functions with altitude (Yuter and Houze, 1995). The CFAD has been calculated based on hourly snapshots. During the stratiform case reflectivity at all vertical levels is strongly overestimated in the CONTROL experiment. Modifying the rain and snow assumptions, but leaving the hail formulations untouched (ExpGRHA experiment) hardly improves this overestimation. Weighting the size distributions of all hydrometeors to those typical of stratiform precipitation (ExpDSGR experiment) brings the simulated reflectivity values closer to the observations (Fig. 7a).

In the upper troposphere, reflectivities in both the ExpGSHA and ExpDSGR are more in correspondence with the observations as compared to the CONTROL. This is due to an improved representation of the snow aggregation effect in these experiments, yielding smaller snowflakes at cold temperatures in the upper troposphere (Fig. 7a). A dramatic increase in the graupel species occurs in the ExpDSGR experiment due to enhanced accretion of cloud water (Pgacw) and the much slower sedimentation velocity of this species (Fig. 3c). As the size distribution of the hail species is now weighted towards low reflective small graupel, these large amounts still result in a reduction of the reflectivity, bringing it closer to the observations.

4.3.2. Convective cases

During the convective cases, many stratiform grid cells appear in between the convective cells in the observations. As our main interest is to evaluate the convective cells only, stratiform precipitation regions were left out in the calculation of the CFADs in both observations and simulations. The separation between convective and stratiform regions was done based on an algorithm detecting high intensity grid cells, reflectivity peaks and neighbourhood to such peaks on horizontal reflectivity cross sections at two elevations, being 2500 and 4000 m above AGL (Steiner et al., 1995; Alvarez and Delobbe, 2009). In both convective cases we calculated the CFADs based on hourly snapshots during the main precipitation period (1400–1800 UTC). Both in the supercell and the multicell case, reflectivity values are overestimated at all vertical levels (Fig. 7b and c) of the CONTROL experiment and storms are simulated too deep. From Table 3 it is clear, however, that the domain maximum simulated reflectivity values agree well with the observed values. In the ExpGRHA, no major differences can be detected in the CFADs or the maximum reflectivity values as compared to the CONTROL, although reflectivities in the upper troposphere tend to be in somewhat better agreement with the observations due to the smaller snowflakes at cold temperatures. In the ExpDSGR experiment, reflectivity values seem to be maximised at a value of about 45 dBZ within the lowest 5000 m above AGL and are also somewhat reduced at higher altitudes. Clearly, the domain and time-averaged maximum reflectivity value is underestimated. Hail/graupel amounts grow dramatically in this experiment due to very strong depletion of cloud water through accretion (Pgacw). As graupel is lofted to higher altitudes, it also grows at these altitudes by accretion of cloud ice (Pgaci) and snow (Pgacs). Even if the amounts of graupel grow an order of a magnitude larger as compared to the hail in the CONTROL experiment, observed maximum reflectivity values cannot be reproduced by this experiment, indicating that at least some large hail should be present in a proper simulation of a strong convective storm.

The findings of our experiments for the convective cases agree well with previous mainly idealised studies focusing on the impact of graupel/hail characteristics on simulations of convective storms. Gilmore et al. (2004) found the graupel amounts to grow dramatically (about 7 times larger) mainly by Pgacw in their experiments in which they varied the constant hail intercept parameter and density over a broad range of values. Using a similar experimental setup, Krueger et al. (1995) found equally large increases in the graupel amount.

Fig. 5. Observed and simulated frequency distribution of cloud optical thickness for (a) 0900–1300 UTC during the stratiform case, (b) 1200–1500 UTC during the supercell convective case and (c) 0600–1600 UTC during the multicell convective case.

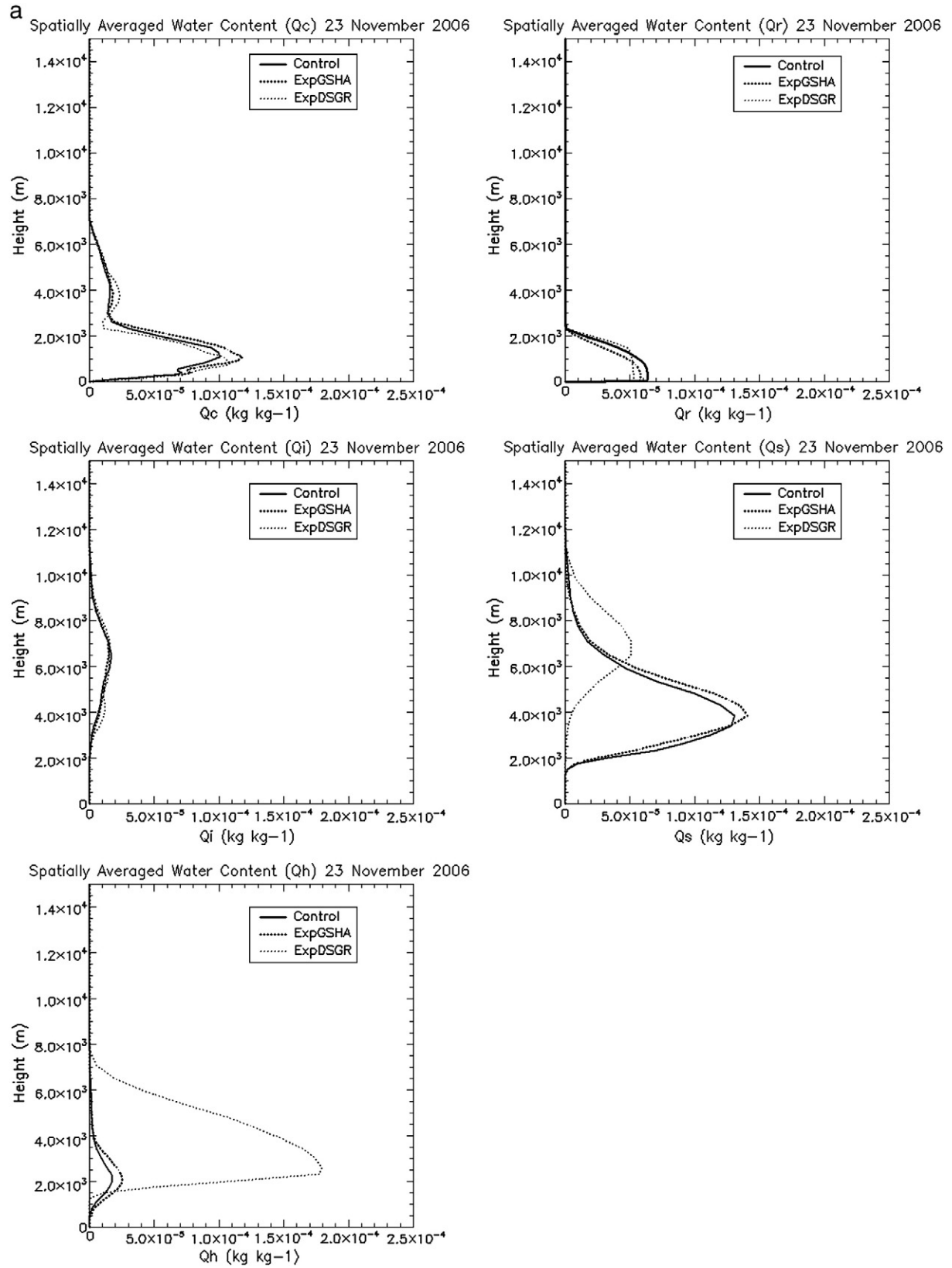

Fig. 6. (a) Domain averaged vertical profiles of cloud water, rain, cloud ice, snow, and hail from 0000–1200 UTC during the stratiform case for all experiments. (b) Domain averaged vertical profiles of cloud water, rain, cloud ice, snow, and hail from 1200–2000 UTC during the supercell convective case for all experiments. (c) Domain averaged vertical profiles of cloud water, rain, cloud ice, snow, and hail from 1200–2000 UTC during the multicell convective case for all experiments.

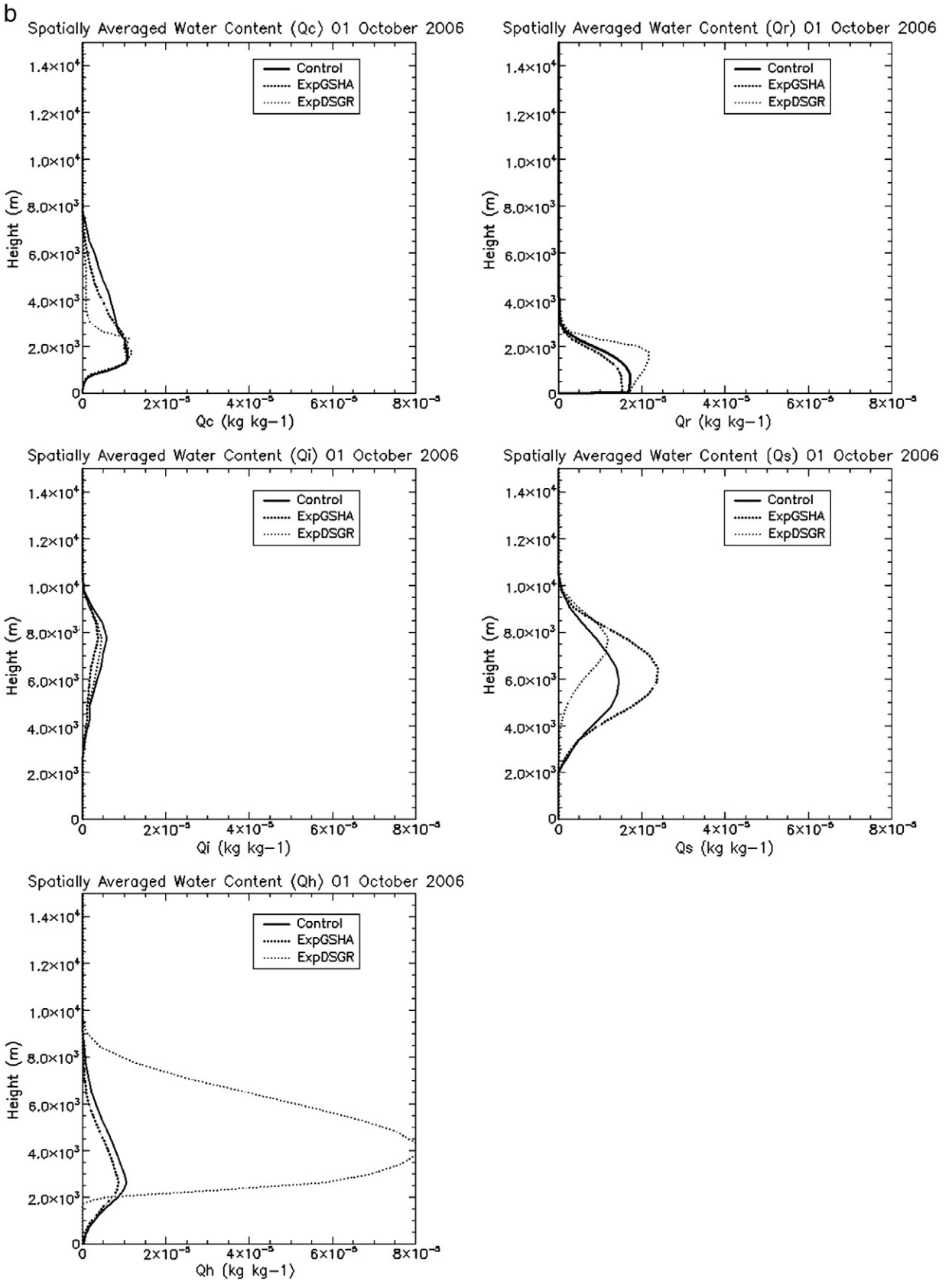

Fig. 6 (*continued*).

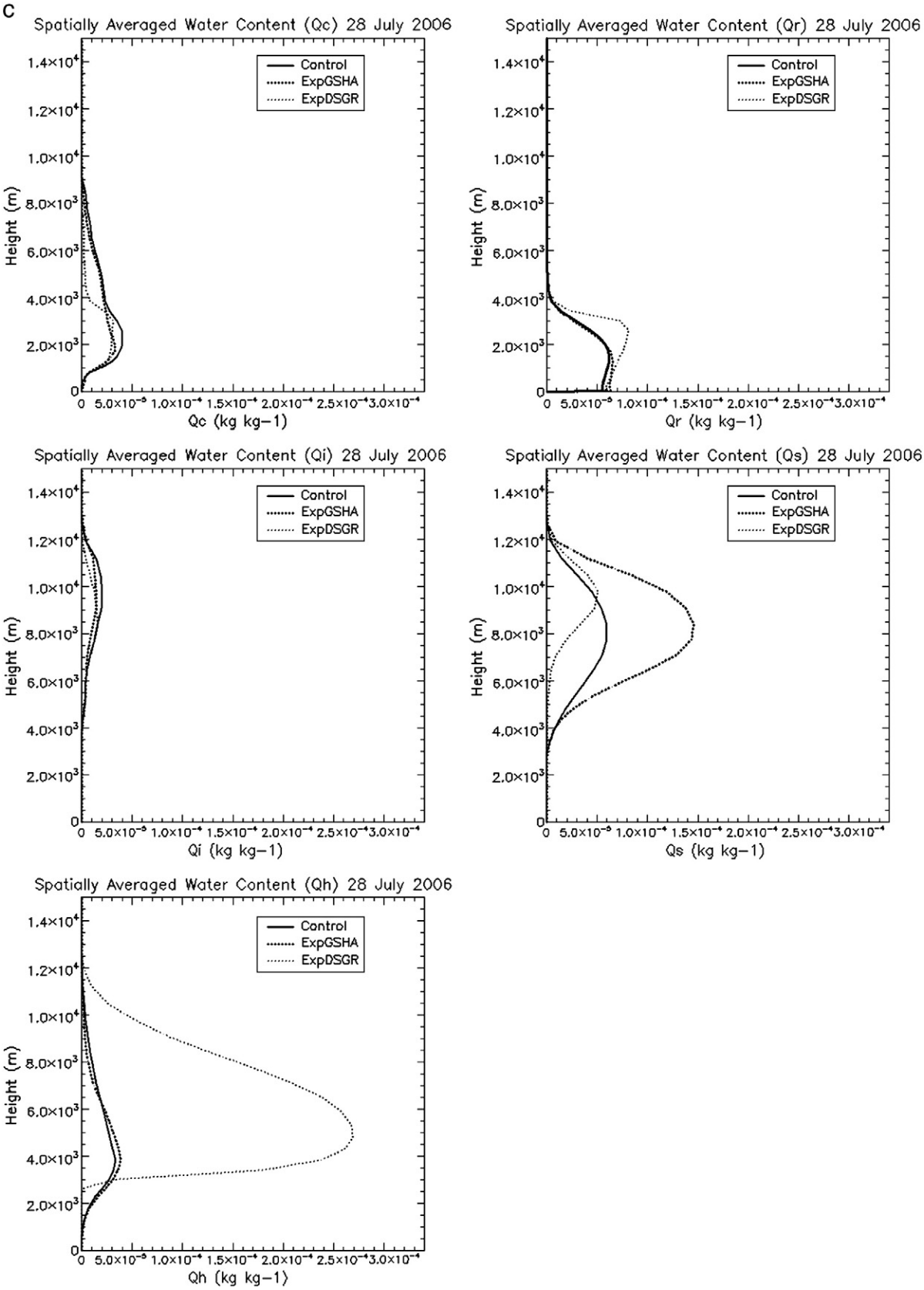

Fig. 6 (*continued*).

4.4. Surface precipitation

4.4.1. Stratiform case

Surface precipitation, which is fallout of rain, snow and hail from the lowest model level, is the ultimate end-product of the microphysical conversions that started with atmospheric vapour consumption. Surface precipitation accumulations over 24 h (0000–2400 UTC) have been calculated for the region within a 150 km radius from the Wideumont radar position in order to be compared against observed radar–rain gauge merged surface precipitation values within the same region. Frequency distribution of the 24 h accumulated surface precipitation is provided in Fig. 8 and domain average and maximum accumulated surface precipitation is provided in Table 3. In order to make a thorough comparison of not only the quantity of surface precipitation, but also of the structure and location of the precipitation field, we implemented a novel verification score that separately considers the structure, amplitude and location errors, referred to as SAL (Wernli et al., 2008). The amplitude component A measures the relative deviation of the domain-averaged simulated precipitation from the observations. Positive values of A indicate an overestimation of total precipitation, whereas negative values indicate an underestimation. For the S and L components, coherent observation objects are separately identified in the simulation and the observations. The location component L combines information about the displacement of the simulated precipitation field's centre of mass and about the error in the weighted-average distance of the precipitation objects from the total field's centre of mass. The structure component S is constructed in such a way that positive values occur if precipitation objects are too large and/ or too flat, and negative values occur if the objects are

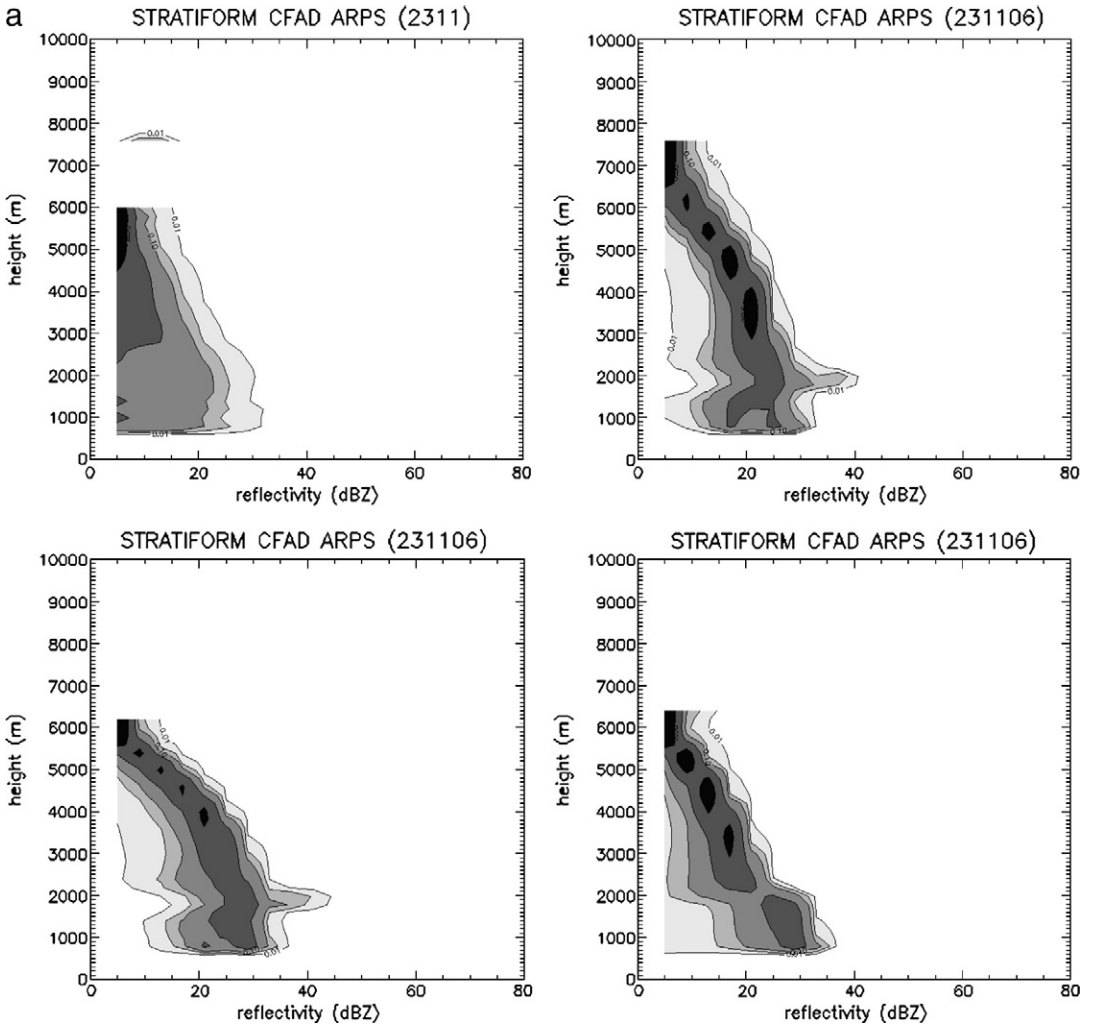

Fig. 7. (a) Domain and time averaged Contour Frequency by Altitude Diagrams (CFAD) as observed by radar (top left) and simulated by the CONTROL (top right), ExpGRHA (bottom left) and ExpDSGR (bottom right) for the stratiform case. (b) Domain and time averaged Contoured Frequency by Altitude Diagrams (CFAD) as observed by radar (top left) and simulated in the CONTROL (top right), ExpGRHA (bottom left) and ExpDSGR (bottom right) experiment for the supercell convective case. Calculation was done solely for cells identified as convective and averaging was done for 1400–1800 UTC with a half hour temporal resolution. (c) Domain and time averaged Contoured Frequency by Altitude Diagrams (CFAD) as observed by radar (top left) and simulated in the CONTROL (top right), ExpGRHA (bottom left) and ExpDSGR (bottom right) experiment for the multicell convective case. Calculation was done solely for cells identified as convective and averaging was done for 1400–1800 UTC with a half hour temporal resolution.

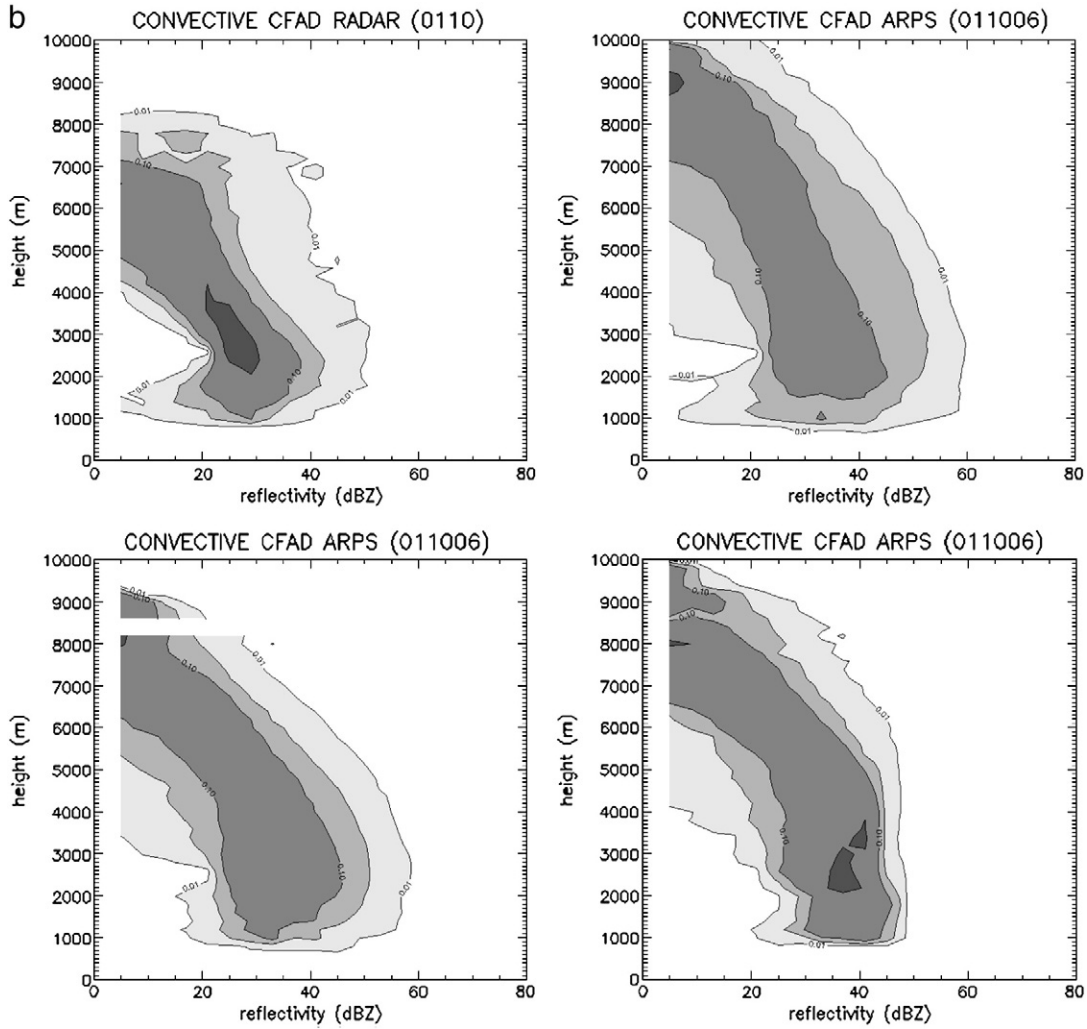

Fig. 7 (*continued*).

too small and /or too peaked. The values of S and A components are within [-2, 2] and of the L component within [0, 2], a zero value yielding a perfect forecast. For a thorough description of the definition of each component we refer to Wernli et al. (2008). All scores calculated for the three cases are summarised in Table 4. CONTROL surface precipitation in the stratiform case is slightly overestimated as compared to the observed precipitation values (Table 3 and A-component in Table 4), although the general distribution is quite well captured (Fig. 8) and the structure and location of the precipitation field are well simulated (Table 4, S and L-components).

In ExpGRHA surface precipitation increases significantly, leading to a 40% overestimation (Tables 3 and 4). The reason for this increase is on the one hand a much larger portion of the precipitation originating from melting of hail (Prmlg) and a decreased fraction originating from melting of snow (Prmls, Fig. 4a) as compared to the CONTROL experiment (most snow is removed above the melting layer due to largely increased Pgacs). This means that the fast pathway of vapour– cloud water/snow – hail – favours more precipitation than the slower pathway of vapour – snow – rain. On the other hand, at low mixing ratios rain falls faster in the ExpGRHA experiment as compared to the CONTROL experiment (Fig. 3). As rain mixing ratios are generally low in this stratiform situation (lower than 1 g kg^{-1}), mean sedimentation velocity is about 50 % larger in the ExpGRHA experiment. Woods et al. (2007) also found increased precipitation rates in the simulation of a wide cold-frontal rainband when applying empirical mass-diameter and velocity-diameter relationships for snow as compared to constant density spheres (their (v only) and (m and v) experiments), although mass-weighted fall velocity of the snow species was reduced. This mostly went together with strong reductions of the liquid water phase aloft and favouring quick glaciation.

In the ExpDSGR experiment surface precipitation is also enhanced as compared to the CONTROL experiment (Table 3), but to a lesser extent as compared to the ExpGSHA. Although the fast falling hail species is not present in this experiment, rain fall speeds are still generally increased as compared to the CONTROL experiment. The structure and location of the

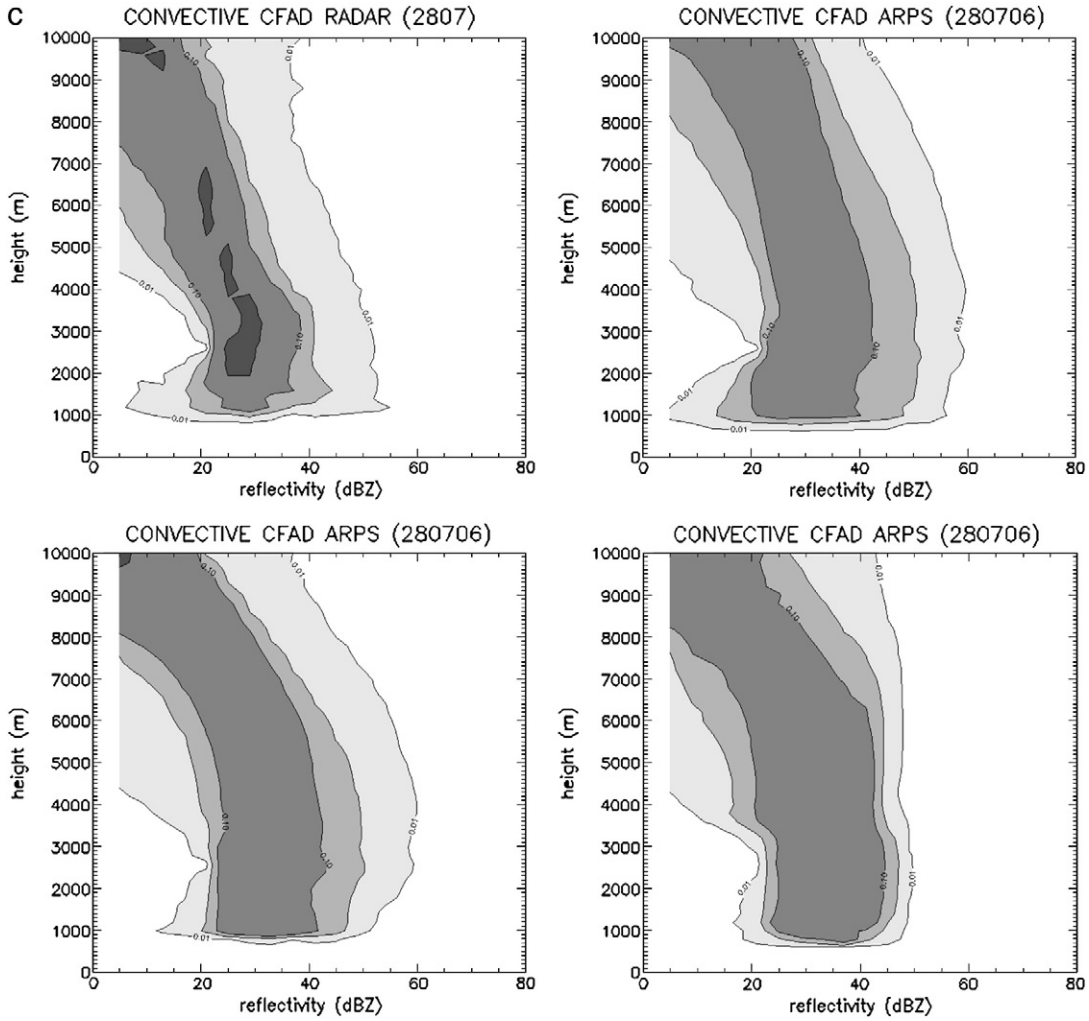

Fig. 7 (*continued*).

Table 3
Comparison between the observed values for reflectivity (Z) and surface precipitation (RR) versus all sensitivity experiments.

	Convective/ stratiform ratio (%)	Max Z (dBZ)	Mean RR (mm day^{-1})	Max RR (mm day^{-1})
Stratiform				
Observed	–	40.8	11.4	38.5
CONTROL	–	42.0	12.6	55.1
ExpGRHA	–	48.9	15.5	56.6
ExpDSGR	–	35.6	13.9	54.5
Supercell				
Observed	0.35	62.8	1.6	35.0
CONTROL	1.50	65.6	3.1	42.5
ExpGRHA	1.50	64.4	2.6	33.3
ExpDSGR	1.22	53.9	2.7	24.9
Multicell				
Observed	0.75	64.4	5.5	100.0
CONTROL	1.27	66.6	11.3	200.4
ExpGRHA	1.25	69.5	11.3	172.6
ExpDSGR	2.03	55.1	12.5	100.7

Observed values of reflectivity are obtained from the volume scan of the C-band weather radar in Wideumont and surface precipitation is obtained from a merged product of radar and rain gauge data using a mean field bias adjustment. Time averaged convective/stratiform rain area ratios are given as well.

precipitation field remain highly unaffected in both the ExpGSHA and ExpDSGR (Table 4).

4.4.2. Convective cases

During the supercell convective case, surface precipitation is overestimated by about 90 % (Table 3) and too widespread in the control simulation leading to large A- and S-components of the SAL analysis (Table 4). In the ExpGRHA experiment, this overestimation is somewhat improved to 60%, while the structure and location remain similar as in the control (Table 4). As can be seen from Fig. 8, the model fails in simulating the many light precipitation grid cells that have been observed. This is mainly because a weak occlusion system in the morning hours was not captured well by the model. However, the model also overestimates the number of grid cells with intense precipitation, indicating too widespread and too intense storms. In a convective case, hail growth takes place to a large extent by accretion of cloud water (Pgacw, Fig. 4b versus a). This means that the presence of large amounts of cloud water actually can enhance precipitation fallout in contrast to the stratiform case where Pgacw is of much less importance. In

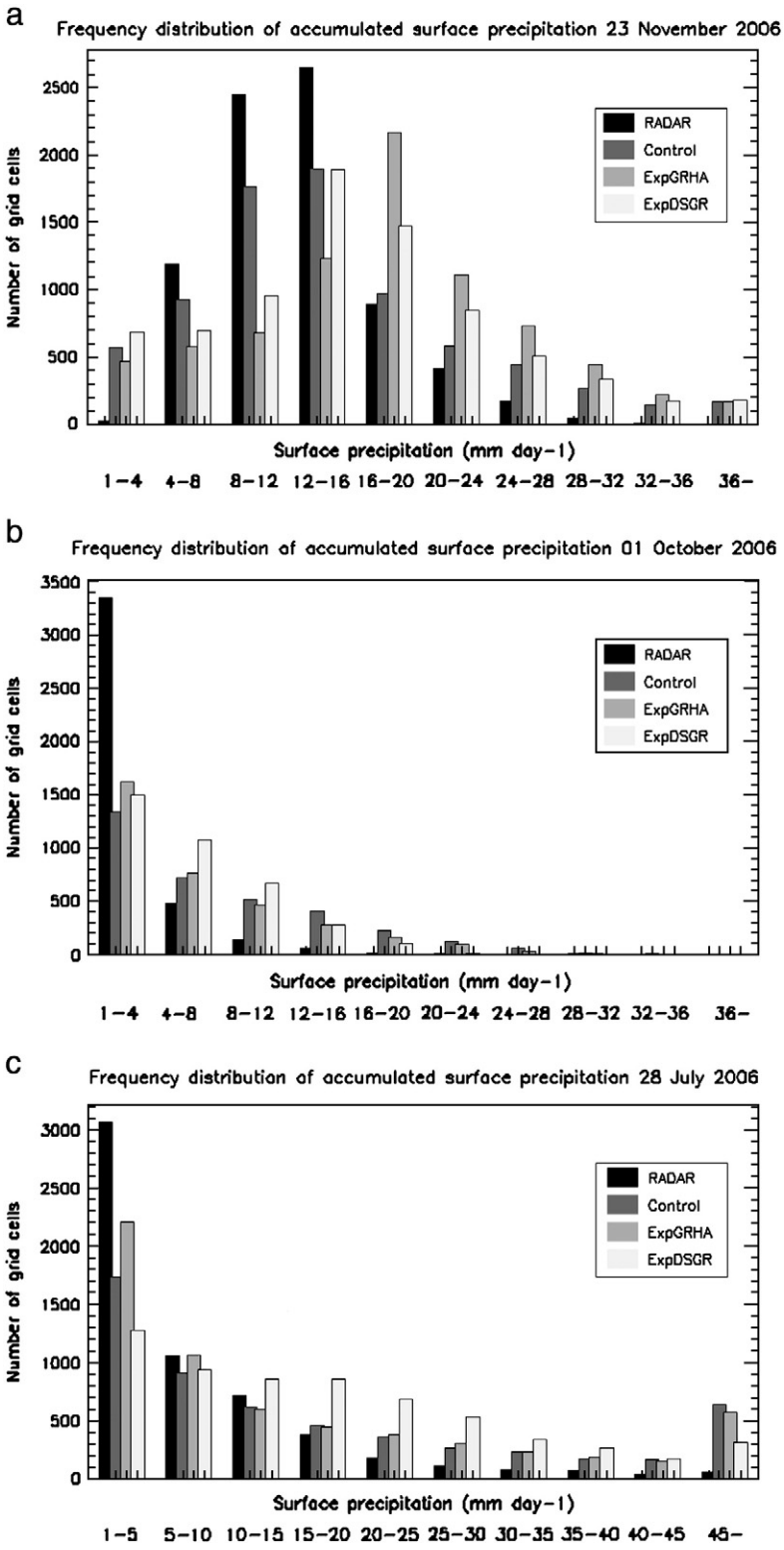

Fig. 8. Observed and simulated frequency distribution of 24 h (0000 UTC–2400 UTC) accumulated surface precipitation for (a) the stratiform case, (b) the supercell convective case and (c) the multicell convective case.

Table 4
Structure (S), Amplitude (A) and Location (L) components of the SAL analysis for 24 h accumulated surface precipitation in the control, ExpGSHA and ExpDSGR and for all cases.

	S	A	L
Stratiform			
CONTROL	−0.16	0.10	0.06
ExpGRHA	0.02	0.30	0.06
ExpDSGR	−0.06	0.19	0.06
Supercell			
CONTROL	1.12	0.64	0.47
ExpGRHA	1.11	0.49	0.45
ExpDSGR	1.81	0.51	0.63
Multicell			
CONTROL	−0.27	0.74	0.23
ExpGRHA	−0.23	0.74	0.14
ExpDSGR	1.71	0.83	0.48

SAL analysis has been applied only on grid cells within 150 km from the radar position.

accreted by hail (Pgacw) and more water will be stored in the snow phase, due to enhanced depositional growth (Psdpv). Furthermore, high intensity rain (having high mixing ratios) falls slower (Fig. 3), leading to decreased peak precipitation (Table 3). So far it is not yet fully understood why exactly less cloud water condensation occurs in the supercell case leading to decreased vapour consumed. We neither found updrafts to be less vigorous nor significantly reduced latent heat release in this experiment (not shown). It might be that the modified rain size distribution assumptions have a significant impact on cold pool dynamics, as suggested by e.g. Dawson et al. (2010). This will be subject of a further investigation.

In the ExpDSGR experiment, surface precipitation overestimation is decreased to the same extent as in the ExpGRHA experiment (Table 3 and Fig. 8), and hence no further improvement of the surface rainfall overestimation takes place, despite the smaller turnover of vapour to condensate discussed in Section 4.1. It could be that this is due to a counteracting effect of enhanced latent heat release associated with the increased riming of cloud droplets on graupel (Pgacw, Fig. 4b) which will be further studied. The maximum 24 h accumulated surface precipitation is decreased significantly and is too low compared to the observed peak precipitation. Furthermore, SAL analysis indicates that the structure of the precipitation field strongly deteriorates as the S-component increases to almost 2. Hence, surface precipitation becomes too widespread when weighting the size distributions of snow and hail towards those typical for stratiform precipitation. Table 3 also provides the relative portion of the precipitation falling as stratiform or convective precipitation, based on the algorithm mentioned in Section 4.3.2. Our experiments suggest that a too large portion falls as convective precipitation during both convective cases. Although the surface precipitation becomes widespread and reflectivity in the ExpDSGR experiment is decreased, the stratiform portion remains too small as compared to the observed stratiform portion. This confirms findings of many other studies such as Zhou et al. (2007) or Morrison et al. (2009).

In the multicell case surface precipitation is altered in a somewhat different way as compared to the supercell case. In the CONTROL experiment both domain average surface precipitation and peak precipitation are about double the amount observed, while the structure of the precipitation field seems to be well captured (Table 4). In contrast to the supercell case, no change in domain average surface precipitation takes place in the ExpGRHA experiment, although peak precipitation is somewhat reduced (Tables 3 and 4). While in the supercell case cloud water condensation was strongly decreased, this is not the case in the multicell case and hence no large difference in the net vapour consumed by the microphysical processes is present.

During the ExpDSGR, surface precipitation is surprisingly increased despite lower net vapour consumption as compared to the other experiments. Sublimation back to the vapour phase is of the same order of importance as compared to the supercell case. The main difference with the supercell case is that upper level winds are very weak in this case and hence storms hardly propagate through the domain. Instead, they develop, mature and decay at about the same location without precipitation being advected out of the domain. As could be seen from Fig. 6c, more precipitating hydrometeors occur in contrast to the other experiments, as much of the cloud phase is collected by graupel. While graupel was effectively advected out of the domain in the supercell case, a larger portion of the graupel eventually is turned to rain in the multicell case (not shown). This leads mainly to an increase of the number of grid cells with intermediate precipitation values (10–30 mm) as can be derived from Fig. 8. Consistent with the supercell case, precipitation becomes too widespread in the ExpDSGR (Table 4) leading to high values of the S-component.

5. Summary and conclusion

The main objective of this research was to determine how moist processes and mainly surface precipitation in a nonhydrostatic mesoscale model are affected by modifications in the size distribution assumptions of a simple 1-moment bulk microphysics scheme. Two sensitivity experiments on the size distribution assumptions of the rain, snow and hail variables were set up for three extreme precipitation cases very different in nature. This was done to understand what the impact was of a model modification made to improve the moist processes under a certain synoptic situation in other synoptic situations. The vapour phase, cloud phase, precipitation phase and surface precipitation were rigorously evaluated against remotely sensed and surface observational data in order to understand if the modifications made in the microphysics scheme brought the simulations closer to the observations or not.

While the net vapour consumption was not much altered by applying size distribution assumptions typical for convective precipitation in both the stratiform and convective cases, including size distribution assumptions weighted to stratiform precipitation strongly decreased the net vapour consumed by the microphysics scheme. It was shown that this is probably related to strongly increased sublimation of graupel back to the vapour phase, associated with its long residence time aloft as it is precipitating much slower than hail.

Cloud optical thickness distribution could only be realistically represented during the stratiform case applying size distribution assumptions typical for stratiform precipitation,

including dendritic snow and graupel. Including graupel led to significantly reduced snow depositional growth and snow collection by graupel, leading to decreased amounts of optically thick snow, while the total amount of precipitating ice (snow + graupel) remained unaffected. In convective cases, cloud optical thickness was also brought closer to the observations by inclusion of graupel, related both to decreased amounts of snow and cloud water. This finding has significant relevance for the radiation budget in numerical models, as the radiative forcing is likely to be better represented in experiments including some graupel.

From comparison of observed and simulated radar reflectivity, it was found that improved rain and snow size distributions do not affect the vertical radar reflectivity profile significantly. However, a proper representation of reflectivity during the stratiform case was impossible without the inclusion of small graupel. During the convective cases, however, the experiments including small graupel are not capable of reproducing realistically the highest reflective cores associated with large hail.

Surface precipitation was found to be far less sensitive to modifications to the size distribution assumptions than cloud optical thickness and radar reflectivity. In all cases, none of the experiments was able to significantly improve a positive surface precipitation bias. Faster rain fall speeds and more rain originating from fast falling hail as compared to slowly falling snow as compared to a control simulation resulted in increased surface precipitation during the stratiform case when rain and snow size distribution assumptions were more realistically represented. This effect was smaller when graupel replaced large hail. During the convective cases, the reasons for modified surface precipitation characteristics in the microphysics experiments were not easy to trace. A slight decrease of surface precipitation was found by both microphysics experiments in a supercell case, while little effect was found in the multicell case. No clear effect was found on updraft intensity or latent heat release, but it will be further studied how cold pool dynamics are affected by the modified rain size distribution. On the other hand, a decrease in the peak precipitation in all experiments is probably related with the slower rain fall speeds. Consistent in both convective cases is that when the size distributions of snow and graupel are weighted towards those typical of stratiform precipitation, the surface precipitation field becomes too widespread, reflected in a high S-component of the SAL analysis.

In this study we applied changes to multiple parameters simultaneously in order to understand the consequences of improved representation of the size distribution characteristics to the representation of moist processes. While we felt to have contributed to some understanding of the implications of such improved size distribution assumptions, it should be stressed that sensitivity studies in which a single parameter is changed in each experiments allow for a more unambiguous interpretation and hence we would recommend such an experimental design in future studies.

Although caution is necessary when drawing broad conclusions from only three case studies, we could summarise that it was found highly advisable to apply graupel formulations when simulating moist processes during a frontal stratiform situation, as both COT and reflectivity could not be simulated properly without. During convective cases, large hail was necessary to capture the very reflective convective cores as well as the surface precipitation structure, although the COT was negatively affected. In general we would advise to include both hail and graupel in an operational numerical weather prediction model, confirming the suggestions of e.g. McCumber et al. (1991) and Cohen and McCaul (2006) to increase the number of ice categories in microphysical schemes. While the cloud phase and vertical reflectivity profiles could be enhanced by modifications presented in the above analysis, important to e.g. realistically represent the surface radiation characteristics, surface rainfall overestimation found in all cases could not be solved by any of the modifications made. This also suggests that simply increasing the number of ice categories or improving the size distribution characteristics in an OMB microphysics scheme by itself might not lead to improvement. While many studies found similarly low sensitivities as found in our experiments, e.g. Gilmore et al. (2004) found surface precipitation to be four times smaller in a simulation having small graupel as compared to large hail. While the vertical wind profile they applied was comparable to the one in our supercell convective case, their storms were much more vigorous and deeper. On the other hand their simulations were rather short (2 h) and their domain was smaller than the one used in our simulations. It should be further investigated whether the differences in the sensitivities found by previous studies and in this research are mainly related to a different experiment's design or to different atmospheric conditions.

Acknowledgements

This research was carried out in the framework of the QUEST-B project, funded by the Flemish Fund for Scientific Research (FWO-Vlaanderen). Furthermore, we would like to acknowledge the Center for Analysis and Prediction of Storms (CAPS) of Oklahoma University for providing the ARPS source code online and Jerry Straka and Ming Xue for fruitful discussions leading to the experiments carried out. Furthermore, we like to thank the Deutscher Wetterdienst (DWD) and the ICSU/WMO World Data Center for Remote Sensing of the Atmosphere for providing the Satellite Application Facility on Climate Monitoring (CM-SAF) and APOLLO satellite derived cloud properties respectively. Atmospheric sounding data were provided by the Department of Atmospheric Science of the University of Wyoming. We are also grateful to the European Environment Agency for making available the CORINE land cover data, the US Geological Survey for the GTOPO30 terrain height dataset, the Deutsches Zentrum für Luft und Raumfahrt (DLR) for the processed AVHRR imagery for sea surface temperature and the Flemish Institute for Technological Research (VITO) for the SPOT vegetation NDVI imagery. This research is conducted utilising high performance computational resources provided by the University of Leuven, http://ludit.kuleuven.be/hpc. Lastly, we appreciate the comments of the anonymous reviewers, improving an earlier draft.

Appendix A

In all conversion terms used in this paper naming convection is used so that the hydrometeor species experiencing the gain (loss) is represented by the first (last) letter. The third and the fourth letter indicate the type of interaction: ev (evaporation), sb (sublimation), cd (condensation), dp (depositional growth), nt (initiation), ac (accretion / collection), f (Bergeron process) and ml (melting). When three species are involved, the third letter indicates the accreting species.

Pvevr	Rain evaporation
Pvsbi	Cloud ice sublimation
Pvsbg	Hail/graupel sublimation
Pvsbs	Snow sublimation
Pvevw	Cloud water evaporation
Pwcdv	Cloud water condensation
Pidpv	Cloud ice depositional growth at the expense of water vapour
Psdpv	Snow depositional growth
Pintv	Initiation of cloud ice at the expense of water vapour
Pidpw	Cloud ice depositional growth at the expense of cloud water
Pihow	Homogeneous freezing of cloud water to cloud ice
Psaui	Autoconversion of cloud ice to snow
P(g)(s)raci	Collection of cloud ice by rain adding to hail/graupel or snow (loss term for cloud ice)
P(g)(s)iacr	Collection of rain by cloud ice adding to hail/graupel or snow (loss term for rain)
Psfi	Depositional growth of snow at the expense of cloud ice due to the Bergeron process
Pgaci	Collection of cloud ice by hail/graupel
Pwmli	Melting of cloud ice to cloud water
Prauw	Autoconversion of cloud water to rain
P(r)sacw	Collection of cloud water by snow adding to rain or snow
Pracw	Collection of cloud water by rain
Pgacw	Collection of cloud water by hail/graupel
Prgacw	Collection of cloud water by hail/graupel adding to rain
Psfw	Depositional growth of snow at the expense of cloud water due to the Bergeron process
Psaci	Collection of cloud ice by snow
Ps(g)acr	Collection of rain by snow adding to hail/graupel or snow
Pgacs	Collection of snow by hail/graupel
Pgaus	Autoconversion of snow to hail/graupel
Pgracs	Collection of snow by rain adding to hail/graupel
Prmls	Melting of snow to rain
Pgacr	Collection of rain by hail/graupel
Pgfrr	Homogeneous freezing of rain to hail/graupel
Prmlg	Melting of hail/graupel to rain

References

Alvarez, M.V., Delobbe, L., 2009. Improvement of radar precipitation estimates using volume reflectivity data and mesoscale model forecast. Internal report MO/34/015, Royal Meteorological Institute of Belgium. 28 pp.

Chevallier, F., Bauer, P., 2003. Model rain and clouds over ocean: comparison with SSM/I observations. Mon. Weather Rev. 131, 1240–1255.

Cohen, C., McCaul, E.W., 2006. The sensitivity of simulated convective storms to variations in prescribed single-moment microphysics parameters that describe particle distributions, sizes, and numbers. Mon. Weather Rev. 134, 2547–2565.

Colle, B.A., Garvert, M.F., Wolfe, J.B., Mass, C.F., Woods, C.P., 2005. The 13-14 December 2001 IMPROVE-2 event: Part III. Simulated microphysical budgets and sensitivity analysis. J. Atmos. Sci. 62, 3535–3558.

Cotton, W.G., Tripoli, G.J., Rauber, R.M., Mulvihill, E.A., 1986. Numerical simulation of the effects of varying ice crystal nucleation rates and aggregation processes on orographic snowfall. J. Appl. Meteorol. 25, 1658–1680.

Cox, G.P., 1988. Modelling precipitation in frontal rainbands. Q. J. R. Meteorol. Soc. 114, 115–127.

Dawson, D.T., Xue, M., Milbrandt, J.A., Yau, M.K., 2010. Comparison of evaporation and cold pool development between single-moment and multimoment bulk microphysics schemes in idealized simulations of tornadic thunderstorms. Mon. Weather Rev. 138, 1152–1171.

Ferrier, B.S., 1994. A double-moment multiple-phase four-class bulk ice scheme: Part I. Description. J. Atmos. Sci. 51, 249–280.

Fu, Q., Liou, K.-N., 1993. Parameterization of the radiative properties of cirrus clouds. J. Atmos. Sci. 50, 2008–2025.

Gilmore, M.S., Straka, J.M., Rasmussen, E.N., 2004. Precipitation uncertainty due to variations in precipitation particle parameters within a simple microphysics scheme. Mon. Weather Rev. 132, 2610–2627.

Goudenhoofdt, E., Delobbe, L., 2009. Evaluation of radar-gauge merging methods for quantitative precipitation estimates. Hydrol. Earth Syst. Sci. 13, 195–203.

Groenemeijer, P.H., van Delden, A., 2007. Sounding-derived parameters associated with large hail and tornadoes in the Netherlands. Atmos. Res. 83, 473–487.

Houze, R.A., Hobbs, P.V., Herzegh, P.H., Parsons, D.B., 1979. Size distributions of precipitation particles in frontal clouds. J. Atmos. Sci. 36, 156–162.

Jiusto, J.E., Bosworth, G.E., 1971. Fall velocity of snowflakes. J. Appl. Meteorol. 10, 1352–1354.

Kain, J.S., Fritsch, J.M., 1993. Convective parameterization for mesoscale models: the Kain-Fritsch scheme. The representation of cumulus convection in numerical models. Meteorol. Monogr. 24, 165–170.

Karlsson, K.-G., Wolters, E., Albert, P., Tetzlaff, A., Roebeling, R., Thomas, W., Johnston, S., 2005. Initial validation of CM-SAF cloud products using MSG/SEVIRI data. Scientific report, Satellite Application Facility on Climate Monitoring, SAF/CM/DWD/SMHI/KNMI/SR/CLOUDS/1. 39 pp.

Khain, Pokrovsky, A.A., Sednev, I., 1999. Some effects of cloud-aerosol interaction on cloud microphysics structure and precipitation formation: numerical experiments with a spectral microphysics cloud ensemble model. Atmos. Res. 52, 195–220.

Kogan, Y.L., 1991. The simulation of a convective coud in a 3D model with explicit microphysics: Part I. Model description and sensitivity experiments. J. Atmos. Sci. 48, 1160–1189.

Krueger, S.K., Fu, Q.A., Liou, K.N., Chin, H.N.S., 1995. Improvements of an ice-phase microphysics parameterization for use in numerical simulations of tropical convection. J. Appl. Meteorol. 34, 281–287.

Lin, Y.-L., Farley, R.D., Orville, H.D., 1983. Bulk parameterization of the snow field in a cloud model. J. Climate Appl. Meteorol. 22, 1065–1092.

Locatelli, J.D., Hobbs, P.V., 1974. Fall speeds and masses of solid precipitation particles. J. Geophys. Res. 79, 2185–2197.

McCumber, M., Tao, W.-T., Simpson, J., Penc, R., Soong, S.-T., 1991. Comparison of ice-phase microphysical parameterization schemes using numerical simulations of tropical convection. J. Appl. Meteorol. 30, 985–1004.

Milbrandt, J.A., Yau, M.K., 2005. A multimoment bulk microphysics parameterization: Part II. A proposed three-moment closure and scheme description. J. Atmos. Sci. 62, 3065–3081.

Morrison, H., Thompson, G., Tatarskii, V., 2009. Impact of cloud microphysics on the development of trailing stratiform precipitation in a simulated squall line: comparison of one- and two-moment schemes. Mon. Weather Rev. 137, 991–1007.

Noilhan, J., Planton, S., 1989. A simple parameterization of land surface processes for meteorological models. Mon. Weather Rev. 117, 536–549.

Ovtchinnikov, M., Kogan, Y.L., 2000. An investigation of ice production mechanisms in small cumuliform clouds using a 3D model with explicit microphysics. Part I: Model description. J. Atmos. Sci. 57, 2989–3003.

Reisner, J., Rasmussen, R.M., Bruintjes, R.T., 1998. Explicit forecasting of supercooled liquid water in winter storms using the MM mesoscale model. Q. J. R. Meteorol. Soc. 124, 1071–1107.

Roebeling, R.A., Feijt, A.J., Stammes, P., 2006. Cloud property retrievals for climate monitoring: implications of differences between Spinning Enhanced Visible and Infrared Imager (SEVIRI) on METEOSAT-8 and Advanced Very High Resolution Radiometer (AVHRR) on NOAA-17. J. Geophys. Res. 111, D20210, doi:10.1029/2005JD006990.

Rutledge, S.A., Hobbs, P.V., 1983. The mesoscale and microscale structure and organization of clouds and precipitation in mid-latitude cyclones: Part VIII. A model for the "seeder-feeder" process in warm-frontal rainbands. J. Atmos. Sci. 40, 1185–1206.

Saunders, R.W., Kriebel, K.T., 1988. An improved method for detecting clear-sky and cloudy radiances from AVHRR data. Int. J. Remote Sens. 9, 123–150.

Schröder, M., van Lipzig, N.P.M., Ament, F., Chaboureau, J.-P., Crewell, S., Fischer, J., Matthias, V., Van Meijgaard, E., Walther, A., Willén, U., 2006. Model predicted low-level cloud parameters: Part II. Comparison with satellite remote sensing observations during the BALTEX Bridge Campaigns. Atmos. Res. 82, 83–101.

Schulz, J., Thomas, W., Müller, R., Behr, H.-D., Caprion, D., Deneke, H., Dewitte, S., Dürr, B., Fuchs, P., Gratzki, A., Hollmann, R., Karlsson, K.-G., Manninen, T., Reuter, M., Riihelä, A., Roebeling, R., Selbach, N., Tetzlaff, A., Wolters,

E., Zelenka, A., Werscheck, M., 2009. Operational climate monitoring from space: the EUMETSAT satellite application facility on climate monitoring (CM-SAF). Atmos. Chem. Phys. 9, 1687–1709.
Seifert, A., Beheng, K.D., 2006. A two-moment cloud microphysics parameterization for mixed-phase clouds: Part 2. Maritime vs. continental deep convective storms. Meteorol. Atmos. Phys. 92, 67–82.
Smedsmo, J.L., Foufoula-Georgiou, E.F., Vuruputur, V., Kong, F., Droegemeier, K., 2005. On the vertical structure of modeled and observed deep convective storms: insights for the precipitation retrieval and microphysical parameterization. J. Appl. Meteorol. 44, 1866–1884.
Smith, P.L., Myers, C.G., Orville, H.D., 1975. Radar reflectivity factor calculations in numerical cloud models using bulk parameterization of precipitation. J. Appl. Meteorol. 14, 1156–1164.
Solomon, A., Morrison, H., Persson, O., Shupe, M.D., Bao, J.W., 2009. Investigation of microphysical parameterizations of snow and ice in Arctic clouds during M-PACE through model-observation comparisons. Mon. Weather Rev. 137, 3110–3128.
Steiner, M., Houze, R.A., Yuter, S.E., 1995. Climatological characterization of three-dimensional storm structure from operational radar and rain gauge data. J. Appl. Meteorol. 34, 1978–2006.
Sui, C.H., Lau, K.-H., Li, X., 1998. Convective-radiative interaction in simulated diurnal variations of tropical cumulus ensemble. J. Atmos. Sci. 54, 637–655.
Sun, W.-Y., Chang, C.-Z., 1986. Diffusion model for a convective layer: Part I. Numerical simulation of convective boundary layer. J. Climate Appl. Meteorol. 25, 1445–1453.
Tao, W.-K., Simpson, J., Baker, D., Braun, S., Chou, M.-D., Ferrier, B., Johnson, D., Khain, A., Lang, S., Lynn, B., Shie, C.-L., Starr, D., Sui, C.-H., Wang, Y., Wetzel, P., 2003. Microphysics, radiation and surface processes in the Goddard Cumulus Ensemble (GCE) model. Meteorol. Atmos. Phys. 82, 97–137.
Thompson, G., Field, P.R., Rasmussen, R.M., Hall, W.D., 2008. Explicit forecasts of winter precipitation using an improved bulk microphysics scheme: Part II. Implementation of a new snow parameterization. Mon. Weather Rev. 136, 5095–5115.
Tong, M., Xue, M., 2008. Simultaneous estimation of microphysical parameters and atmospheric state with simulated radar data and ensemble square root Kalman filter: Part I. Sensitivity analysis and parameter identifiability. Mon. Weather Rev. 136, 1630–1648.
Waldvogel, A., 1974. The N0 jump of raindrop spectra. J. Atmos. Sci. 31, 1067–1078.
Wernli, H., Paulat, M., Hagen, M., Frei, C., 2008. SAL – a novel quality measure for verification of quantitative precipitation forecasts. Mon. Weather Rev. 136, 4470–4487.
Wisner, C., Orville, H.D., Myers, C., 1972. A numerical model of a hail-bearing cloud. J. Atmos. Sci. 29, 1160–1181.
Woods, C.P., Stoelinga, M.T., Locatelli, J.D., 2007. The IMPROVE-1 storm of 1–2 February 2001: Part III. Sensitivity of a mesoscale model simulation to the representation of snow particle types and testing of a bulk microphysical scheme with snow habit prediction. J. Atmos. Sci. 64, 3927–3948.
Xue, M., 2000. High-order monotonic numerical diffusion and smoothing. Mon. Weather Rev. 128, 2853–2864.
Xue, M., Droegemeier, K.K., Wong, V., 2000. The Advanced Regional Prediction System (ARPS) – a multi-scale nonhydrostatic atmospheric simulation and prediction model: Part I. Model dynamics and verification. Meteorol. Atmos. Phys. 75, 161–193.
Xue, M., Droegemeier, K.K., Wong, V., Shapiro, A., Brewster, K., Carr, F., Weber, D., Liu, Y., Wang, D., 2001. The Advanced Regional Prediction System (ARPS) – a multi-scale nonhydrostatic atmospheric simulation and prediction tool: Part II. Model physics and applications. Meteorol. Atmos. Phys. 76, 143–165.
Yuter, S.E., Houze, R.A., 1995. 3-dimensional kinematic and microphysical evolution of Florida cumulonimbus: 1. Spatial-distribution of updrafts, downdrafts and precipitation. Mon. Weather Rev. 123, 1941–1963.
Zhang, G., Xue, M., Cao, Q., Dawson, D., 2008. Diagnosing the intercept parameter for exponential raindrop size distribution based on video disdrometer observations: model development. J. Appl. Meteorol. Climatol. 47, 2983–2992.
Zhou, Y.P., Tao, W.-K., Hou, A.Y., Olson, W.S., Shie, C.-L., Lau, K.-M., Chou, M.-D., Lin, X., Grecu, M., 2007. Use of high-resolution satellite observations to evaluate cloud and precipitation statistics from cloud-resolving model simulations: Part I. South China Sea Monsoon Experiment. J. Atmos. Sci. 64, 4309–4329.